Neutrino Signatures in Terrestrial Detectors from Two- and Three-Dimensional Core-Collapse Supernova Simulations

A Thesis Presented for the

Master of Science

Degree

The University of Tennessee, Knoxville

Tanner Brooks Devotie

December 2015

To my wife, Chalea...

Acknowledgements

I would like to thank Dr. Bronson Messer for providing excellent advice, encouragement and many good laughs throughout the process of completing this work. I would like to extend this thank you to Dr. Raph Hix and Dr. Eric Lentz who were always more than happy to provide helpful conversation and valuable insight during my research. I would also like to thank Dr. Thomas Papatheodore, Dr. Austin Harris and Ryan Landfield for their help, encouragement and kindness throughout my time with the group. I extend a very special thank you to Dr. Marianne Breinig for always believing in me and encouraging me to pursue this degree. Finally, I thank my family and wife, Chalea, for their patience and encouragement through the good and difficult times of my graduate career.

Abstract

Core-collapse supernovae (CCSNe) are driven by neutrino emission and are the most prodigious sources of neutrinos in the Universe. Importantly, the neutrino radiation from CCSNe is emitted from deep in the explosion and can provide information about physical processes taking place in the newly-born neutron star at the heart of the event. We examine the four-flavor (i.e. ν_e, $\bar{\nu}_e$, ν_x and $\bar{\nu}_x$) [electron, muon, and tau neutrinos along with their anti-matter counterparts] signature of CCSNe neutrino emission in various neutrino detector types. We use data from the multidimensional Chimera (Lentz et al., 2015) code (from both 2D and 3D simulations) and use the SNOwGLoBES package (Beck et al., 2013) to model detector responses to a fiducial galactic CCSNe event at 10 kpc [kiloparsecs]. We find that low resonance MSW [Mikheyev-Smirnov-Wolfenstein] effects conspire with the flavor and energy dependence of neutrino-sphere depth to produce dominant signals from two- and three-dimensional simulations that are almost indistinguishable. Other channels exhibit differences, many of which can be ascribed to supernova dynamics.

Table of Contents

List of Figures

Chapter 1

Introduction

Supernovae represent the end of a star's life and the birth of an exotic stellar remnant. The focus of this thesis will be on supernovae produced by the collapse of an iron core in stars more massive than our parent star (10 $M_{\odot}$ or more). These explosions are spectacular events that can outshine their parent galaxy in brightness. Moreover, with these explosion comes a torrent of neutrinos that can tell us a great deal about the mechanisms within the star that cause it to explode. With the help of simulation generated data from Chimera (Lentz et al., 2015) and the software package SNOwGLoBES (SG) (Beck et al., 2013), the neutrino signatures associated with core-collapse supernovae (CCSNe) can be studied in great detail. Here, a brief overview of the types of supernovae and what can be gained from studying the neutrinos produced by them will be provided.

1.1 Supernovae

Observations divide supernovae into at least two types: Type-I and Type-II. The former have no observable hydrogen lines and the latter have strong hydrogen lines. Although there are now many subtypes grouped into these classifications, observers retain this convention of generally either Type-I or Type-II supernova. The following overview is organized after Evan O'Conner's dissertation thesis and proper credit must go to him (O'Connor, 2012) for that structure and helpful references.

Type-Ia supernovae are thermonuclear explosions of carbon-oxygen white dwarfs and compose ∼24% of all supernovae according to the Lick Observatory Supernova Search (LOSS) (Li et al., 2011). As we will see, these types of supernovae are physically different in mechanism and structure than those progenitor stars that produce Type-II supernovae.

Type-Ib and Type-Ic supernovae differ only in their observed absorption lines and are distinguished from Type-Ia from the lack of silicon II lines. We find that Type-Ib progenitor stars have shed the hydrogen shell either through their own stellar wind or perhaps through a companion star at some point in their evolutionary process. Type-Ic progenitors are similar in that they have shed their hydrogen layer followed by the helium layer. Although these layers are lost, the core of the progenitor stars will undergo the CCSN scenario as their hydrogen-rich couterparts. These types correspond to ∼19% of all supernovae according to the LOSS survey (Li et al., 2011).

Type-II Plateau (P) supernovae are the most common and make up ∼40% of all supernovae and ∼70% of Type-II supernovae according to LOSS. This sub-category is identified by the presence of a luminosity plateau (e.g. a graph of luminosity vs. time) phase lasting approximately 100 days. This plateau occurs as the photosphere begins to slowly recede in mass behind the expanding hydrogen envelope at the edge of the star. The star eventually undergoes the "normal" exponential light curve decay expected of a Type-II supernova afterwards. The progenitors are thought to be red supergiants that contain large hydrogen envelopes with a ZAMS (zero age main sequence) mass between ∼8-15 $M_\odot$ (Smartt et al., 2009).

Type-IIb supernovae constitute what is referred to as a "transitional" supernova. The progenitor stars exhibit strong hydrogen lines expected from these types, however after an short period of time, the hydrogen lines disappear and the supernovae enters the aforementioned transitional stage. According to the LOSS survey, these transitional types make up ∼12% of all Type-II supernovae. This suggests there is an important evolutionary channel leading to the Type-IIb supernova that we have yet to fully understand (Claeys et al., 2011; Woosley et al., 1994).

Type-IIn supernovae make up ∼9% of Type-II supernovae in the LOSS survey. They exhibit very narrow emission lines, which are interpreted to mean the light emitting material is slow moving. Moreover, this points to the circumstellar material (i.e. material surrounding the star) being excited by the interaction with the supernova shock wave. It is inferred that the large amount of this material that is lost from the progenitor star happens very close to the time of collapse (Kiewe et al., 2012).

Type-II Linear (L) supernovae exhibit a linear decline in their light curve as opposed to the plateau discussed above and consist of ∼12% of Type-II supernovae in the LOSS survey. Their progenitor stars are thought to be yellow supergiants (Elias-Rosa et al., 2010) that can be extremely luminous (Miller et al., 2009), but little else it known about them. The progenitor stars could have a lighter hydrogen envelope and higher overall mass.

In summary, we see that Type-I and Type-II supernovae represent two progenitor scenarios that differ in both mechanism and physical structure. Furthermore, we clearly see there is some variety in how a supernova can appear when it explodes via core-collapse of an iron core, depending on its exterior structure. Type-I b/c supernovae progenitors have lost their hydrogen (or hydrogen and helium) envelope. Type-IIP contain large hydrogen envelopes near the point of collapse. Type-IIn supernovae progenitors have lost an enormous amount of material in a small period of time preceding the explosion and Type-IIL give a nice slow decay of the light curve eventually leading to the core-collapse. No matter the intermediate path, the massive progenitor stars all explode due to collapse of the iron core. Figure 1.1 gives a visual representation of the CCS model.

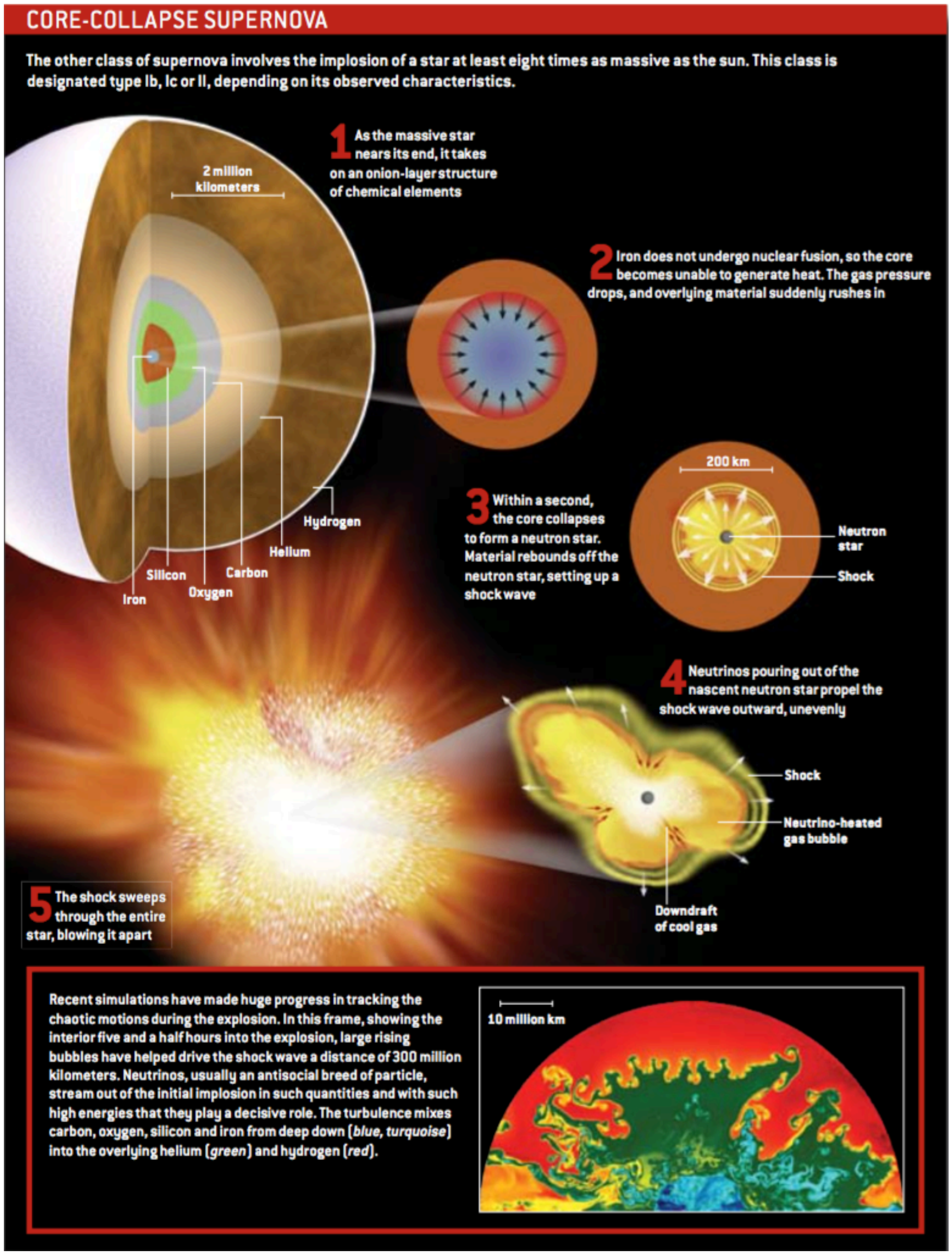

Figure 1.1: Core-Collapse Supernova (from Hillebrandt et al. (2006))

1.2 Core-Collapse

Progenitor stars that undergo the collapse of an iron core (see Figure 1.1) generally have a zero age main sequence (ZAMS) masses of at least 8-10 $M_{\odot}$. Core-collapse supernovae begin when the core of the progenitor star becomes unstable against gravitational collapse; the point where electron degeneracy of the growing iron core can no longer support the weight of the star. This instability is due to the star exhausting all other energy sources. With the fusion of iron nuclei requiring more energy to fuse than is gained from the reaction, the energy output from fusion in the core is now too little to provide the needed pressure to prevent the star from collapsing on itself. The maximum mass of a degenerate core is referred to as the Chandrasekhar mass and is determined by Y_e - the ratio of electrons per nucleon. This varies with stars, but with a ZAMS mass between 8-100 $M_\odot$, the limit can hover around 1.0-1.4 $M_\odot$. The entire evolution of the massive star will imprint the end product supernova. The reader is referred to Woosley et al. (2002), Limongi and Chieffi (2006) and Paxton et al. (2011) for a more detailed discussion of massive stellar evolution.

The collapse time of the progenitor star can be on the order of 100-500 ms with the core separating into two sections: an inner core collapsing homologously because it is in sonic contact and an outer core falling at supersonic speeds. The collapsing core only halts when nuclear densities (i.e. the density of neutrons and protons inside atomic nuclei) are attained. This causes the equation of state to stiffen and ultimately halts the collapse of the inner core causing the outer core to rebound. With the kinetic energy of the rebound (or bounce), there is now an outward propagating pressure wave until it reaches the sonic point (the point where velocity of the material exceeds the velocity of sound in that material), at which time it becomes a shock wave. The resulting shock wave will ultimately blow the star apart. In core-collapse theory, it is important to describe how this shock wave causes the explosion. Although there have been many suggestions as to the driving mechanism behind the explosion, only the neutrino-driven explosion will be explored here.

1.3 Neutrino-Driven Explosion

How a star accomplishes the explosion has remained a mystery for quite some time. What we do know is that for high mass stars, the shock stalls (around 100 km) and becomes an accretion shock (i.e. velocity of shock is approximately zero) (Kitaura et al., 2006). This is due to the pressure behind the shock not being adequate to overcome the ram pressure of the in-falling material. Two mechanisms work to reduce this pressure. First, as material falls through the shock, it slows, converting its kinetic energy into internal energy. Part of this internal energy is then used to dissociate heavy iron-group nuclei into free neutrons, protons and α-particles while also softening the equation of state. Secondly, the emission of neutrinos carries off thermal energy, further reducing the pressure behind the shock. Without the shock wave to drive the star apart, matter will continue falling onto the proto-neutron star (PNS), causing it to collapse further.

In the search for how neutrinos drive the explosions of supernovae, simulations have predominately shown that a neutrino-heating region develops behind the stalled shock wave originally caused by the bounce. This can be visualized as the second to last stage of the explosion itself (see Figure 1.2). From 1.2, we see in the first stage, collapse has begun and electron neutrinos (ν_e) are being emitted as usual. The second stage, labelled "Neutrino Trapping," show that neutrinos are beginning to be trapped by the dense material falling inward. This is due to the neutrinos mean free path (i.e. how far each one travels before interacting) becoming significantly shorter than the radius of the PNS. The third stage, "Bounce and Shock Formation," shows the point where the matter densities reach that of the atomic nucleus and the equation of state stiffens, producing the shock. The fourth stage, "Shock Propagation and ν_e Burst," represent the shock wave propagating outward and also the ν_e burst we expect from simulations as the PNS has become transparent to neutrinos. The fifth stage, "Shock Stagnation and ν Heating," show the shock wave stalling. It is after this stage that the shock is reenergized so as to drive the explosion to its conclusion.

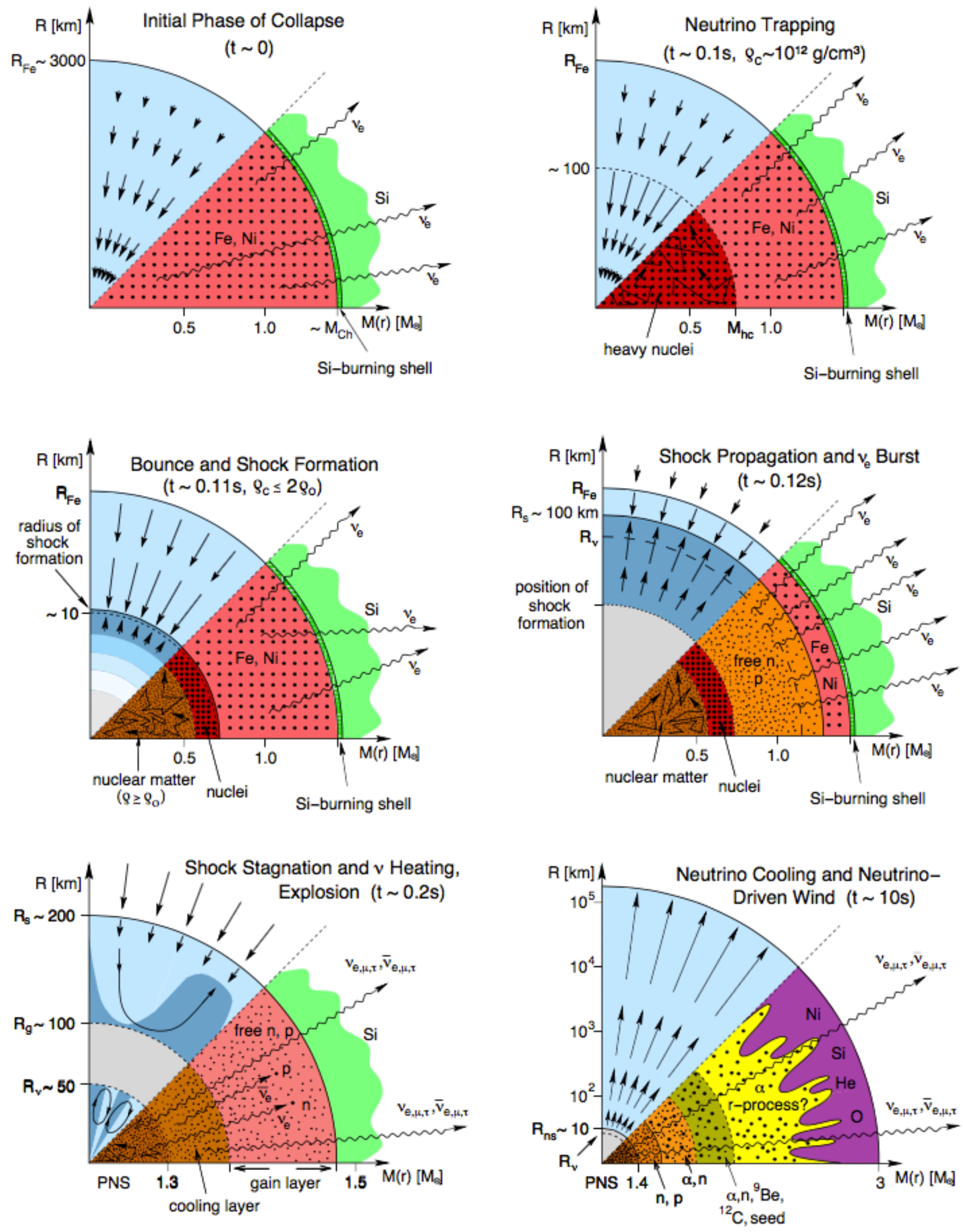

Figure 1.2: Schematic Representation of CCS Evolution (from Janka et al. (2007))

The stage is now being set for the neutrinos to drive the shock to its conclusion. The neutrinos coming coming off the PNS carry most of the energy released by the gravitational collapse of the stellar core (Burrows, 1990). This energy is deposited in the layers between the PNS and the stalled shock, primarily via charged-current ν_e and $\bar{\nu}_e$ captures on free nucleons (Burrows, 1990),

$$\nu_e + n \rightarrow e^- + p, \tag{1.1}$$

$$\bar{\nu}_e + p \rightarrow e^+ + n. \tag{1.2}$$

This is the "neutrino-heating" that will increase the pressure behind the shock. The persistent energy given by the neutrinos serves to keep the pressure high and drive the shock outward again, eventually leading to a supernova explosion.

What can the neutrinos tell us about the progenitor star or stellar corpse left behind? According to O'Connor (2012), the luminosity as a function of time, the spectral shape and flavor content change with time (as we will see later). These changes can be matched with theory governing current progenitor models that could shed light on nuclear equations of state and neutrino oscillations. However, as O'Connor (2012) says, decoupling these details is very difficult. Another possibility as put forth by Brandt et al. (2011) and Lund et al. (2010) is the temporal variation of neutrino signal that are coincident with gravitational wave signatures (Ott et al., 2012). This coincidence could reveal information on the fluid motions within the PNS and post-shock region. Furthermore, neutrino oscillations, via the MSW effect, can lift the curtain on density structure in the early stages of post-explosion as discussed by Duan and Kneller (2009). These are but a few of the benefits of studying neutrino signatures. The reader is referred to those publications for more detail.

Chapter 2

Method

2.1 Chimera

Chimera is a multi-dimensional physics code built to simulate supernovae as laid out by Bruenn et al. (2009). It is broken into three separate codes; 1.) Hydrodynamics and gravity, 2.) Neutrino transport and opacities and 3.) Nuclear equation of state and reaction network. These codes are tied together via a management layer that oversees data management, parallelism, I/O, and control. The hydrodynamics are implemented via a dimensionality split, Lagrangian-remap (PPMLR) scheme (Colella and Woodward, 1984). Self-gravity is computed by multipole expansion (Müller and Steinmetz, 1995), but replacing the Newtonian monopole with a GR monopole (Marek et al. (2006), Case A). Neutrino transport is computed in the 'ray-by-ray-plus' (RbR+) approximation (Buras et al., 2003), where an independent, spherically symmetric transport solve is computed for each angular "ray" (θ-zone). Within the code, each flavor of neutrino is evolved along with their anti-matter counterparts on a 20 point energy grid ranging from 2-250 MeV. The reader is referred to Bruenn et al. (2009) and Lentz et al. (2015) for more detail.

2.2 Neutrinos and SNOwGLoBES

An important clue to our understanding of supernovae is the detection of the neutrino signature generated by such an event. To aid researchers in understanding this particular aspect of supernovae, a software package was developed called SNOwGLoBES: SuperNova Observatories with GLoBES (SG) (Beck et al., 2013). A brief overview of how the software is used and what it produces will now be given.

The SG package makes use of the GLoBES front-end software (Huber et al., 2005). This is shown by figure 2.1.

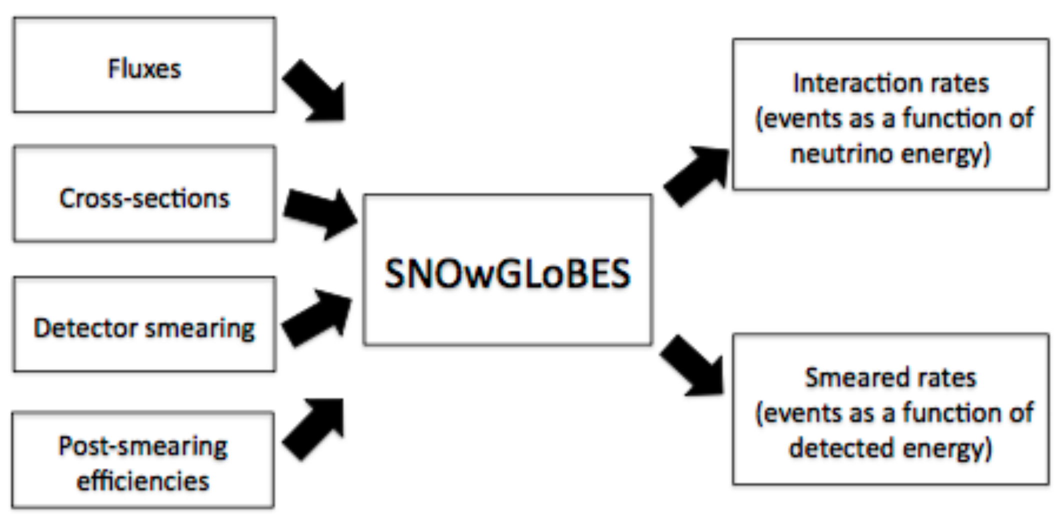

Figure 2.1: SNOwGLoBES Data Flow (Beck et al., 2013)

The package allows the user to perform fast, informative studies into the physics of supernova neutrino detection. The software computes expected event rates by using input fluxes in conjunction with given cross-sections of detectors. The output takes the form on interactions rates for each channel for a given detector detector as a function of neutrino energy and "smeared" (or detected) energy (Beck et al., 2013). The aforementioned computations are only completed once the appropriate data has been fed into the software package. This step will be further explain in the following sections.

Currently, the SG package includes cross-sections and parameterized detector responses for water, argon, scintillator and lead-based configurations as well as two example data sets for neutrino luminosities. Before laying out the reaction channels, we will first present a brief background on the detectors. This background material borrows heavily from Scholberg (2012).

Water Cherenkov Detectors: Neutrinos, having an aversion to matter interactions, naturally require large detectors to detect even a few at a time. Water, being relatively inexpensive, stands as strong choice for detector material due to an abundance of free protons which can interact with neutrinos via inverse beta decay (detailed in next section). Charged particles are detected via the Cherenkov light emitted, of which also forms a 42° cone for relativistic particles detected by photo-multiplier tubes (PMTs) that fill the inside of the detector. This allows the observer to reconstruct the direction vector of the neutrino via the Cherenkov ring pattern. The limit of detection for electrons is 0.8 MeV and 1,400 MeV for protons. A disadvantage in using this material is that particles must have speeds exceeding c/n, where n is the index of refraction for the material ($\sim$1.34 for water). Past examples of this type of detector are the IMB (Becker-Szendy et al., 1993) and Kamiokande (Hirata et al., 1991) made famous by the SN1987A observation. Currently, the only large water Cherenkov detector is Super-K (Ikeda et al., 2007) in Japan. Proposed detectors for water Cherenkov include the Long-Baseline Neutrino Experiment (LBNE) (Akiri et al., 2011), Hyper-Kamiokande (Abe et al., 2011) and MEMPHYS (Borne et al., 2011).

Argon Detectors: Also known as "Liquid Argon Time Projection Chambers (Liquid Argon TPCs)", exhibit very good sensitivity to ν_e via the charged-current (CC) interaction, $\nu_e + {}^{40}\mathrm{Ar} \rightarrow e^- + {}^{40}\mathrm{K}^*$. This allows deexcitation γ rays to be tagged and observed from the interaction. The interaction involving $\bar{\nu}_e$ can also be tagged via $\bar{\nu}_e + {}^{40}\mathrm{Ar} \rightarrow e^+ + {}^{40}\mathrm{Cl}^*$ and subsequent deexcitation γ-rays. Neutral-current interactions typically aren't taken into account due to insufficient information concerning cross sections and observables in literature. Lastly, there are also elastic scattering event between neutrinos and electrons. The detector functions by utilizing large TPCs, where and ionized charge is drifted via an electric field onto a wire plane. This method allows detection of time of arrival of charge at the planes, enabling reconstruction of a three-dimensional track. Particles can be further identified by the rate of energy loss along the track. Along with the above, argon can also scintillate and thus, the detectors are lined with PMTs as a water Cherenkov detector would be. This allows fast timing of signals along with enhancing event localization within the detector. This type of detector allows for good energy resolution along with particle reconstruction without the aforementioned Cherenkov threshold. A current example is ICARUS in Italy (Bueno et al., 2003).

Scintillator: Like water Cherenkov detectors, scintillator detectors utilize large volumes of the liquid scrutinized by PMTs covering the inside of the detector. They are composed of hydrocarbons of the form C_nH_{2n}. The PMTs detect light emitted via deexcitation of molecular energy levels and large numbers of photons being released. This allows the observer to detect energy loss, which is proportional to the amount of photons detected. Furthermore, the interaction vertices can be reconstructed through time of arrival information for the photons. Scintillator detectors allow excellent energy resolution and low thresholds due to the large number of photoelectrons being collected for a standard PMT density. As in water, the dominant detection channel for scintillator detectors is inverse beta decay (IBD). Current examples of such a large volume detector are KamLAND (Eguchi et al., 2003) in Japan and Borexino (Cadonati et al., 2002; Monzani, 2006) in Italy.

Lead: Detectors that employ heavy nuclei have the promise of producing high count rates in both CC and NC interactions (Fuller et al., 1999; Engel et al., 2003; Hargrove et al., 1996; Boyd et al., 2003; Zach et al., 2002) through observing leptons or ejected nucleons. Single- and multi-neutron ejections are also possible. Due to cross sections for the aforementioned neutron ejections being dependent on the neutrino energy, we can measure the relative rates of these processes which enable inference of the incoming neutrino spectra. Specifically, lead is most promising due to its stability and easy of handling in large amounts. Lead's most abundant isotopes also posses a low capture cross section for neutrons. This makes the detectors nearly transparent to supernova-neutrino-induced neutrons. The only example of a lead-based detector is HALO in Canada (Scholberg, 2012).

2.3 Detection Channels

Inverse Beta Decay: IBD ($\bar{\nu}_e + p \rightarrow e^+ + n$) is the dominant detection method for detectors such as water and scintillator where there is an abundance of free protons. The two included water Cherenkov configurations are both 100 kilotons. One has 30% coverage of high quantum efficiency (HQE) photomultiplier tubes and the other has 15% coverage. The former is similar to Super-Kamiokande I (or III, IV), with 40% coverage while the latter is similar to Super-Kamiokande II, with 19% coverage. The scintillator configuration represents 50 ktons of material.

Neutrino-Electron Elastic Scattering: For all detector configurations, the elastic scattering ($\nu_e, \nu_x + e^- \rightarrow \nu_e, \nu_x + e^-$) of neutrinos is important, but perhaps less so for lead-based detectors due to very low observable counts.

Interactions with Oxygen: Interactions with oxygen are performed through charged-current (CC) and neutral-current (NC) interactions. The former with
$\nu_e + {}^{16}\mathrm{O}^* \rightarrow e^- + {}^{16}\mathrm{F}$ and $\bar{\nu}_e + {}^{16}\mathrm{O} \rightarrow e^+ + {}^{16}\mathrm{N}$. Here, the final state can include ejected nucleons, de-excitation gammas and the produced lepton. The latter interaction,
$\nu_x + {}^{16}\mathrm{O} \rightarrow \nu_x + {}^{16}\mathrm{O}^*$, should produce observable de-excitation gammas.

Interactions with Carbon: ν_e can interact with carbon nuclei via CC or NC interactions. The former with $\nu_e + {}^{12}\mathrm{C} \rightarrow {}^{12}\mathrm{N} + e^-$ and $\bar{\nu}_e + {}^{12}\mathrm{C} \rightarrow {}^{12}\mathrm{B} + e^+$.

The NC interaction, $\nu_x + {}^{12}\mathrm{C} \rightarrow \nu_x + {}^{12}\mathrm{C}^*$, produces a 15.5 MeV de-excitation γ-ray that is used to identify the interaction.

Interactions with Argon: For this iteration of the package, only CC interaction, $\nu_e + {}^{40}\mathrm{Ar} \rightarrow e^- + {}^{40}\mathrm{K}^*$ and $\bar{\nu}_e + {}^{40}\mathrm{Ar} \rightarrow e^+ + {}^{40}\mathrm{Cl}^*$ are included. NC interactions, $\nu_x + {}^{40}\mathrm{Ar} \rightarrow \nu_x + {}^{40}\mathrm{Ar}^*$, are not included due to lack of information in the literature (Beck et al., 2013).

Interactions with Lead: CC and NC interactions are included for single and double neutron ejection: $\nu_e + {}^{208}\mathrm{Pb} \rightarrow e^- + {}^{208}\mathrm{Bi}^*$, $\nu_x + {}^{208}\mathrm{Pb} \rightarrow \nu_x, + {}^{208}\mathrm{Pb}^*$ and $\bar{\nu}_x + {}^{208}\mathrm{Pb} \rightarrow \bar{\nu}_x, + {}^{208}\mathrm{Pb}^*$.

Cited within Beck et al. (2013) are the sources of smearing matrices and cross-sections for individual detector configurations. In the interest of brevity, I will leave a more detailed look at these intricacies to the reader. SNOwGLoBES is simply a user-friendly way to use GLoBES (Huber et al., 2005).

2.4 Data Preparation

This section will detail how the CHIMERA data was utilized with SNOwGLoBES (SG) to produce neutrino spectra that resemble what an Earth-based detector should detect from a core-collapse supernova. The bulk of this project was spent creating the "machinery" needed to properly prepare date from CHIMERA (Lentz et al., 2015) to be analyzed by SG. This required extensive use of the software package MATLAB (2015) to manipulate the data as required by the SG manual (Beck et al., 2013). Once prepared, the SG software is used to analyze the data and create a simulated spectra that an Earth-based detector should see in the event of a supernova. Finally, MATLAB (2015) is once again used for processing the large amounts of data generated by SG into manageable directories and produce meaningful plots.

Data Structure: The data from CHIMERA (Lentz et al., 2015) is split between two and three dimensional simulations that are angle-averaged (i.e. the luminosity is averaged over all angles and not taken "ray-by-ray") over the simulated supernova.

To better organize the neutrino data output from CHIMERA, the neutrino spectra are separated into "snapshot" files. The files are moments in time that represent the evolution of the supernova (~0-450 ms). This corresponds to 1,282 / 2,717 files for 2D and 3D simulations respectively, giving a detailed view of neutrino luminosity from the onset of collapse to ~450 ms afterward.

Naturally, the structure of each file is identical. The beginning lines of each file display information about the location of the file, the specific simulation it represents, the time it is taken (i.e. seconds into the supernova simulation), general information about the star and the radius from the center of the star the neutrino luminosities are "detected." The main body of each file displays the neutrino luminosity on a specific energy grid (20 rows of data) ranging logarithmically from roughly 2-250 MeV. The neutrino luminosities are shown in four columns per energy, for each flavor; ν_e, $\bar{\nu}_e$, ν_x and $\bar{\nu}_x$. Here ν_x represents the ν_μ and ν_τ neutrinos; $\bar{\nu}_x$ representing their anti-matter counterparts. These are grouped together due to their luminosities being effectively the same value during the simulation because CHIMERA does not contain physics that differentiate between ν_μ and ν_τ. The units of the neutrino luminosities are given as number/second/MeV. The last bit of information stored within the files are the summed total of each neutrino flavor column (number/second) and their respective root mean square (RMS) energy (MeV). For a more detailed overview of all aspects related to CHIMERA, see Bruenn et al. (2009) and Lentz et al. (2015).

Data Preparation - Overview: SNOwGLoBES requires neutrino luminosity data to be of a certain format before it can be analyzed; 501 rows and 7 columns per data file fed into SG. The first column being energy in 0.0002 GeV steps from 0 to 1 GeV. Columns 2-7 are the neutrino "fluence" (number of neutrinos) of ν_e, ν_μ, ν_τ, $\bar{\nu}_e$, $\bar{\nu}_\mu$ and $\bar{\nu}_\tau$ in that order. For CHIMERA, repeated values of ν_x represent ν_μ and ν_τ; $\bar{\nu}_x$ representing the anti-matter counterparts. Obtaining the units for fluence simplifies to integrating the neutrino luminosities, per time slice, over the entire supernova simulation (~450 ms). This is accomplished by multiplying each neutrino luminosity (i.e. interpolated neutrino luminosity as we will see) by the time interval between the current time slice and the next time slice given by the CHIMERA data (Lentz et al., 2015). Yet another consideration is the distance from the star to the detector on Earth. CHIMERA neutrino luminosities are recorded at a fiducial distance of 1000 km. Thus, the final term slotted into the simple equation takes into account the standard distance of 10 kiloparsecs for the detector-star distance. The equation is now of the following form:

$$Fluence = \frac{1}{4\pi R^2} * \nu * \delta t. \tag{2.1}$$

Here, ν represents any neutrino flavor number luminosity. When calculated, we have taken into account the distance from the star to the Earth-based detector and the time integration leaving only a "fluence" with units of *number of neutrinos per* cm^2.

Recall that each of the CHIMERA data files contain 20 rows of data with the energy ranging from 2-250 MeV. Thus, another task will be to identify a method of interpolation to "fill in the gaps" of our data to fit the criteria of SNOwGLoBES. Since SG requires data to be in steps of 0-1 GeV or 0-100 MeV, we are effectively neglecting the highest energy neutrino data contained within each file of CHIMERA data. Ordinarily, this would certainly be an issue. For the models considered here, the neutrino luminosities above ∼105 MeV were at least 20 orders of magnitude lower than peak luminosities. This tells us there are very, very few neutrinos available to be detected above this energy compared to the overall amount. Thus, we can safely neglect this high energy neutrino data for the purposes of this project. To test this, the number of neutrinos were counted up to 105 MeV as well as beyond this mark up to 4 significant figures. The total count before and after was constant as expected.

Interpolation of CHIMERA *Data:* As mentioned, our first task is to find an appropriate method of interpolation for the CHIMERA data. The purpose of the interpolation is to infer the neutrino luminosities between the already established energy grid CHIMERA uses. This inference allows us to produce the required structure SG specifies. There are two main checks used to decided if a method of interpolation is a sound choice or not: 1.) Does the equation used fit the data from CHIMERA (more on that soon), and 2.) Do we lose or gain neutrinos after interpolating the data (neither should happen).

Our first choice was given by Raffelt et al. (2003) in the form of the following equation termed the "alpha fit":

$$f(E) \propto E^{\alpha} exp[-(\alpha+1)E/\bar{E}]. \tag{2.2}$$

Here, α refers to the "pinch factor", and is defined as the amount the peak in the luminosity vs. energy plot for a neutrino flavor is pulled or pushed apart (i.e. the lower the number, the more pinched; α=2-5 according to Raffelt et al. (2003)).

When testing this equation against the above criteria, the only information we do not posses already is the pinch factor, α, and the associated constant of proportionality. These were found using the MATLAB (2015) "fminsearch" function. The energy and luminosity information are fed into the search function from CHIMERA and an initial guess for the pinch factor and constant are supplied by the user. MATLAB then performs the necessary calculations to minimize the function according to these initial guesses. The pinch factor and constant being the only variable in the calculations, they were varied extensively for any perceived difference. As expected, the lower the value for our pinch factor guess (α), the more "pinched" the peak. The opposite was true for increasing the initial guess for α. The varying of the constant of proportionality was limited to the upper range of the neutrino number luminosities ($10^{53} - 10^{56}$) and had minimal effect on whether or not the equation fit the CHIMERA data. Unfortunately, this method did not produce a plot that fit the CHIMERA data well enough to be used. Later in this section, a plot (figure 2.2) will be shown displaying this particular fit along side the fit we chose overlaid on the CHIMERA data.

The next method tested was linear interpolation given by Deserno (2004). A prerequisite to using this method was to create the appropriate energy grid suitable for use in SG. This meant creating a grid of 501 entries from 0-100 MeV in 0.2 MeV steps; termed the "bin" energy grid. This new grid gives the structure needed to interpolate between the values given in each CHIMERA data file. The equation for linear interpolation is

$$\frac{x_2 - x}{x - x_1} = \frac{1}{f} - 1. \tag{2.3}$$

Here, x_1 and x_2 represent the preceding and following energy or neutrino luminosity mark respectively on the new energy grid. The first step is to determine the scaling factor, f, associated with each value of x (explained below). This first step would look like,

$$f = \frac{1}{1 + \frac{E_2 - x}{x - E_1}} \tag{2.4}$$

where x represents the "bin" energy. This value ranges from 0-100 MeV. This means E_1 and E_2 must also change with each iteration and represent energies from the CHIMERA data. Now that we have found the scaling factor, f, we can now calculate the neutrino luminosity at a specific "bin" energy. This step has the form,

$$x = f x_2 + (1 - f) x_1. \tag{2.5}$$

In the preceding equations, x represented "bin" energies. Here, x, x_1 and x_2 will represent the neutrino luminosities and f, the scaling factor we calculated previously. The next consideration we have are the magnitude of separation between the scaling factor, f, and number luminosity. Recall that energy in each CHIMERA file ranges from ~2-250 MeV while the number luminosities can range from $10^{30} - 10^{56}$ in magnitude. Thus, this must be taken into account when calculating the larger range of luminosities (luminosities associated with the "bin" energy grid). To do this, we first take the *log* (linear in the log interpolation) of the luminosities within the equation (x_1 and x_2) to bring the orders of magnitude into reasonable agreement with the scaling factor f. Next, we exponentiate the equation to bring all terms back to the expected order of a neutrino luminosity (i.e. $10^{30} - 10^{56}$ number/second/MeV). This is the general outline of interpolating neutrino luminosities linearly, effectively "filling in the gaps" in the CHIMERA data to suit the current requirements of SG.

This particular routine is performed on each CHIMERA data file (1,282 / 2,717 files for 2D and 3D simulations respectively). As it turns out, the linear in the log interpolation method fits the data from CHIMERA better than the alpha-fit. Figures 2.2, 2.3 and 2.4 show the CHIMERA data, alpha fit and linear interpolation on a single plot. The first figure is the data as a whole. The second figure shows a zoomed area around the peak while the third figure shows the zoomed area around the tail.

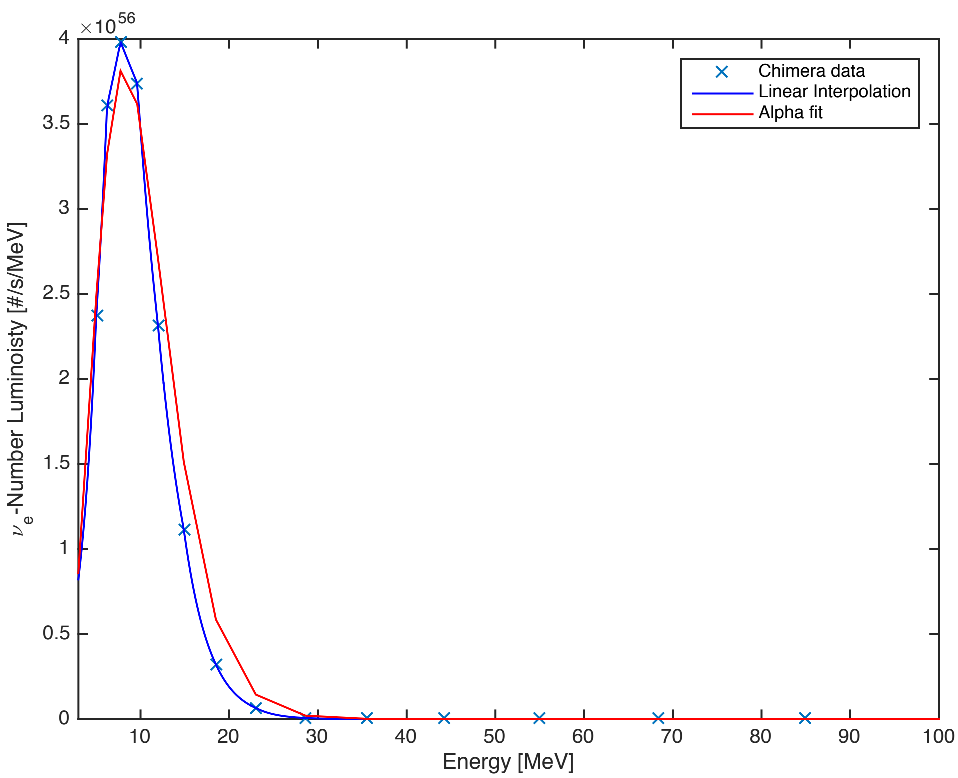

Figure 2.2: CHIMERA data, Alpha fit and Linear Interpolation Comparison

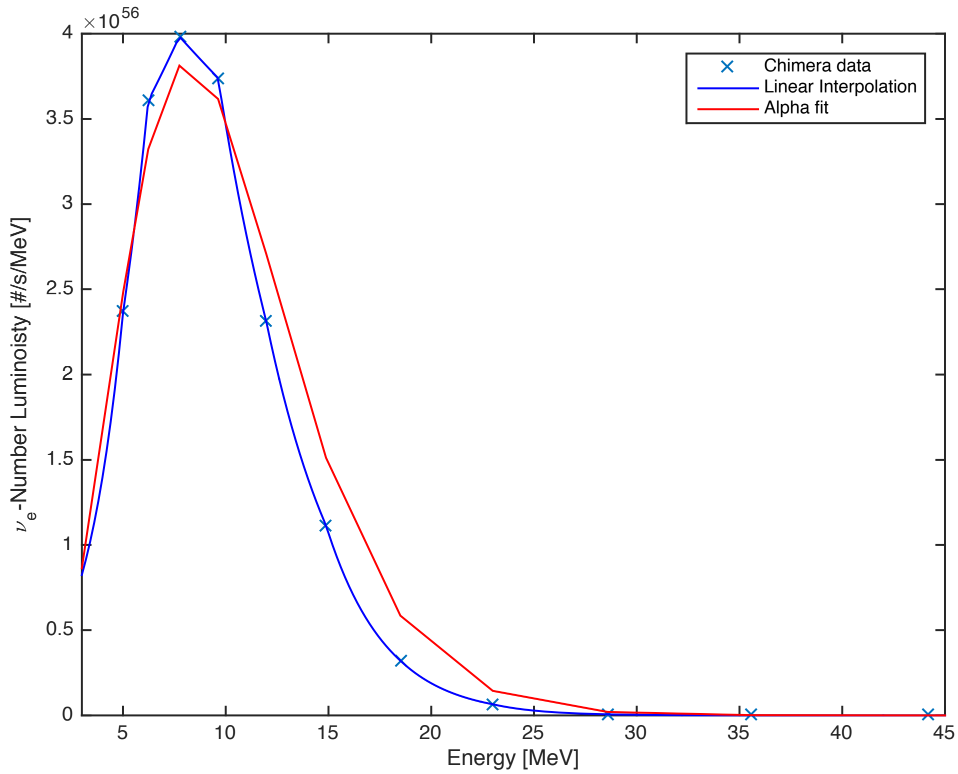

Figure 2.3: Interpolation Comparison - Peak Zoom

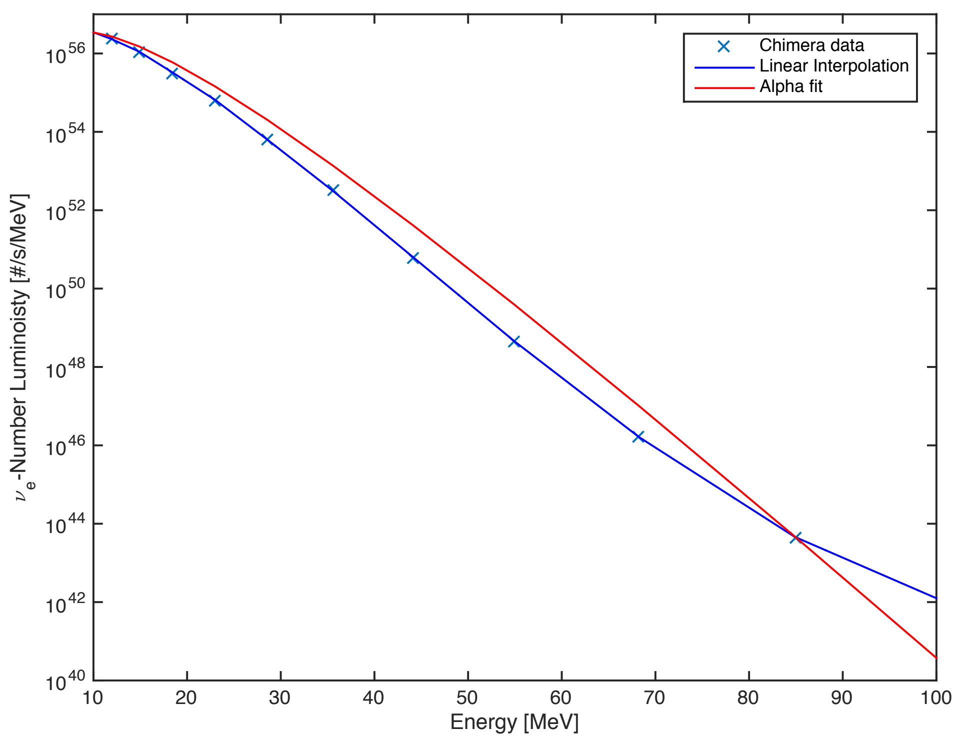

Figure 2.4: Interpolation Comparison - Tail Zoom

2.5 Oscillation

With the above considerations, neutrino luminosity data can now be passed to SNOwGLoBES (Beck et al., 2013). This will produce neutrino signature data relevant for detectors that consist of argon, water, scintillator and lead. However, we know that neutrinos oscillate due to the mixture of flavor and mass eigenstates (Mirizzi et al., 2015) and so should expect the neutrino signature data generated up until this point to be incorrect in that it does not portray true neutrino behavior. Our task now is to include what we know about neutrino oscillation to build a neutrino signature that is as correct as our understanding allows. First, I will attempt to give an overview of the methods of oscillation and why we did or did not choose them. Next, I will provide a detailed derivation of how we computed neutrino oscillations to another flavor as compared to Dighe and Smirnov (2000) contributions in the field.

There are two means of neutrino oscillation that are important in the core of the supernova; "collective effects" and "MSW (a.k.a. matter mediated) effects" (Janka et al., 2007). Each have their region of effect along the line of sight to the supernova. Collective effects describes how neutrinos forward scatter off other neutrinos inducing coherent flavor oscillation. This effect is limited to immediately around the PNS due to high neutrino densities in this region. This is because as the density increases, the mean free path of the neutrinos becomes shorter than the radius of the PNS and the region immediately outside it. This allows the neutrino density to rise, allowing neutrino-neutrino interaction and forward scattering. We chose to neglect this method due to insufficient understanding of collective effects in the literature. Furthermore, at early times, which the Chimera simulations are performed, the PNS and region immediately surrounding it exhibits a very high optical depth which causes decoherence of the neutrinos (Chakraborty et al., 2011).

MSW effects (a.k.a Mikheyev-Smirnov-Wolfenstein or matter mediated effects) describes how neutrinos interact with matter (mostly electrons) as they travel out from the core of the supernova and induce oscillation to another flavor. This effect occurs in either a high or low (or both) resonant density region (Lund and Kneller, 2013; Dighe, 2008). The former is characterized by a density of $\rho_H \sim 10^3 g/cm^3$ ($\Delta m^2_{atm}, \theta_{13}$) and the latter by $\rho_L \sim 10 g/cm^3$ ($\Delta m^2_{\odot}, \theta_{12}$) (Dighe, 2008). Oscillations in these regions are governed by the adiabaticities of the resonant density regions, which are directly affected by the neutrino mixing angle. Although the accepted mixing angle (θ_{13}) is large enough to be considered adiabatic, it is too small to cause coherent oscillations (Chiu et al., 2013; Dighe, 2008). Furthermore, Lund and Kneller (2013) show that stars in the range of ~10-18 $M_{\odot}$ (comparable to Chimera simulations) take ~1 second or more for the shock to reach the high resonance region where a density gradient and thus, coherent scattering can occur. Our Chimera simulations confirm this. This forces the MSW effects at high resonance to be neglected for this work. However, low resonance is always adiabatic and will always induce oscillation via neutrino interactions on matter. This will be the only source of oscillation we consider for this work.

In this section a detailed derivation and explanation of the equations used to calculate the neutrino oscillation in vacuum are provided. First, I discuss the equations taken as standard (Dighe and Smirnov, 2000). Second, I discuss the equations we chose to begin from (Kneller, 2015). Finally, I show that these are equivalent.

Neutrino masses can obey either a normal hierarchy (NH) or an inverted hierarchy (IH). These labells refer to how the masses of the neutrinos are organized versus the flavor eigenstates. For the normal hierarchy, the flavor eigenstates of the neutrinos follow the normal mass hierarchy of the corresponding leptons; ν_e's are the lightest, ν_μ's are second and ν_τ's are the heaviest. In the inverted hierarchy, the ordering is changed slightly. No longer does the mass hierarchy of the corresponding lepton flavor dictate the ordering. Rather, the arrangement shown in Figure 2.5 obtains. This reflects the fact that we know only the size of Δm^2_{13} and the size and sign of Δm^2_{12} (Chiu et al., 2013). The equations from Dighe and Smirnov (2000) are:

Normal Hierarchy

$$N_{\nu_e} = N_{\nu_x} \tag{2.6}$$

$$N_{\bar{\nu_e}} = \cos^2(\theta_\odot) N_{\bar{\nu_e}} + \sin^2(\theta_\odot) N_{\nu_x} \tag{2.7}$$

$$4N_{\nu_x} = \cos^2(\theta_\odot) N_{\nu_x} + \sin^2(\theta_\odot) N_{\bar{\nu_e}} + N_{\nu_e} + 2N_{\nu_x} \tag{2.8}$$

Inverted Hierarchy

$$N_{\nu_e} = \sin^2(\theta_\odot) N_{\nu_e} + \cos^2(\theta_\odot) N_{\nu_x} \tag{2.9}$$

$$N_{\bar{\nu_e}} = N_{\nu_x} \tag{2.10}$$

$$4N_{\nu_x} = \sin^2(\theta_\odot) N_{\nu_x} + \cos^2(\theta_\odot) N_{\nu_e} + N_{\bar{\nu_e}} + 2N_{\nu_x} \tag{2.11}$$

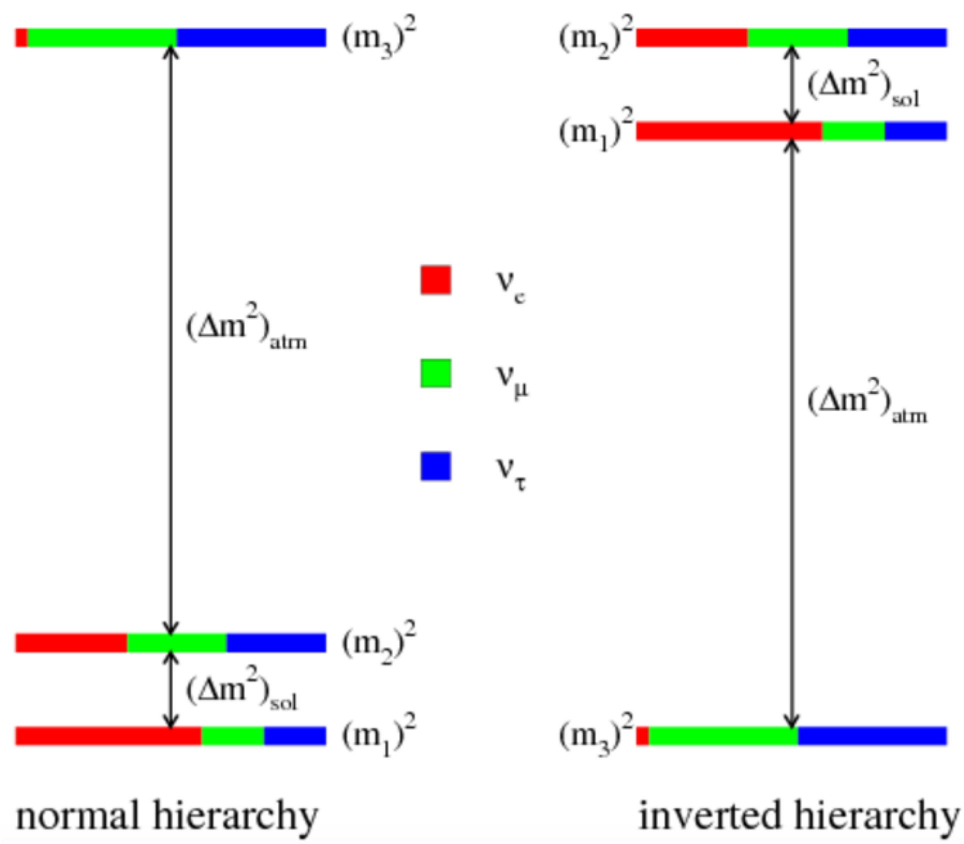

Figure 2.5: Normal and Inverted Hierarchy Comparison (from Hew (2012))

Here, N represents the number of neutrinos and ν_x represents ν_μ, ν_τ, $\bar{\nu_\mu}$ and $\bar{\nu_\tau}$ combined. This is an important distinction because the data from Chimera distinguishes between ν_x and $\bar{\nu_x}$. The importance of this will be pointed out again during the derivation. The last variable, $\theta_\odot$, represents θ_{12} and it termed the mixing angle. We chose to use a value of 0.591 radians (33.86°) from Chiu et al. (2013). Kneller (2015) cast neutrino oscillations for normal hierarchy in the following form:

$$F_e(R) = \frac{1}{4\pi R^2}[p_{ee}(R_\nu)\Phi_e(R_\nu) + (1 - p_{ee}(R_\nu))\Phi_x(R_\nu)] \tag{2.12}$$

$$F_\mu(R) + F_\tau(R) = \frac{1}{4\pi R^2}[(1 - p_{ee}(R_\nu))\Phi_e(R_\nu) + (1 + p_{ee}(R_\nu))\Phi_x(R_\nu)] \tag{2.13}$$

$$\bar{F}_e(R) = \frac{1}{4\pi R^2}[\bar{p}_{ee}(R_\nu)\bar{\Phi}_e(R_\nu) + (1 - \bar{p}_{ee}(R_\nu))\bar{\Phi}_x(R_\nu)] \tag{2.14}$$

$$\bar{F}_\mu(R) + \bar{F}_\tau(R) = \frac{1}{4\pi R^2}[(1 - \bar{p}_{ee}(R_\nu))\bar{\Phi}_e(R_\nu) + (1 + \bar{p}_{ee}(R_\nu))\bar{\Phi}_x(R_\nu)] \tag{2.15}$$

There are two key differences here compared to the equations of Dighe and Smirnov (2000): 1) The inclusion of the R^{-2} factor taking into account the detector is located at Earth (or 10 kiloparsecs), and 2) The units of the equation. Equations 2.12 - 2.15 are taken to have units of $number * sec^{-1} * cm^{-2}$, or flux. The two variables $p_{ee}/\bar{p}_{ee}$ and $\Phi(R_\nu)$ represent survival probabilities and neutrino luminosities ($number * sec^{-1}$) respectively. The neutrino luminosities are provided from our interpolation results while the survival probabilities can be found by comparing the equations from Kneller (2015) and Dighe and Smirnov (2000) pair wise. For example, if we compare equations 2.6 and 2.12, it can quickly be concluded that, for the flux of ν_e neutrinos to completely oscillate to ν_x neutrinos, p_{ee} must equal zero. If we then compare equations 2.7 and 2.14, we can see that, for NH, $\bar{p}_{ee}$ must equal $\cos^2(\theta_{12})$ ($\theta_{12} = \theta_\odot$). If we substitute these terms into equations 2.12 - 2.15 we get the following:

$$F_e(R) = \frac{1}{4\pi R^2}[\Phi_x(R_\nu)] \tag{2.16}$$

$$F_\mu(R) + F_\tau(R) = \frac{1}{4\pi R^2}[\Phi_e(R_\nu) + \Phi_x(R_\nu)] \tag{2.17}$$

$$\bar{F}_e(R) = \frac{1}{4\pi R^2}[\cos^2(\theta_{12})\bar{\Phi}_e(R_\nu) + (1 - \cos^2(\theta_{12}))\bar{\Phi}_x(R_\nu)] \tag{2.18}$$

$$\bar{F}_\mu(R) + \bar{F}_\tau(R) = \frac{1}{4\pi R^2}[(1 - \cos^2(\theta_{12}))\bar{\Phi}_e(R_\nu) + (1 + \cos^2(\theta_{12}))\bar{\Phi}_x(R_\nu)] \tag{2.19}$$

Substituting trigonometric identities we then have,

Normal Hierarchy

$$F_e(R) = \frac{1}{4\pi R^2}[\Phi_x(R_\nu)] \tag{2.20}$$

$$F_\mu(R) + F_\tau(R) = \frac{1}{4\pi R^2}[\Phi_e(R_\nu) + \Phi_x(R_\nu)] \tag{2.21}$$

$$\bar{F}_e(R) = \frac{1}{4\pi R^2}[\cos^2(\theta_{12})\bar{\Phi}_e(R_\nu) + \sin^2(\theta_{12})\bar{\Phi}_x(R_\nu)] \tag{2.22}$$

$$\bar{F}_\mu(R) + \bar{F}_\tau(R) = \frac{1}{4\pi R^2}[\sin^2(\theta_{12})\bar{\Phi}_e(R_\nu) + \bar{\Phi}_x(R_\nu) + \cos^2(\theta_{12})\bar{\Phi}_x(R_\nu)] \tag{2.23}$$

As can be seen, equations 2.20 and 2.22 now resemble equations 2.6 and 2.7. To show that equations 2.21 and 2.23 resemble equation 2.8 is our next task. This can be done by adding equation 2.21 and 2.23 together which gives the following:

$$F_\mu + F_\tau + \bar{F}_\mu + \bar{F}_\tau = \frac{1}{4\pi R^2}[\Phi_e + \Phi_x + \sin^2(\theta_{12})\bar{\Phi}_e + \bar{\Phi}_x + \cos^2(\theta_{12})\bar{\Phi}_x] \tag{2.24}$$

This obviously does not quite match equation 2.8. However, recall that Dighe and Smirnov (2000) define ν_x to include ν_μ, ν_τ, $\bar{\nu_\mu}$ and $\bar{\nu_\tau}$ while Chimera distinguishes between ν_x and $\bar{\nu}_x$. Dighe and Smirnov (2000) effectively assumes that $\Phi_x = \bar{\Phi}_x$. With this assumption, we find equation 2.24 has the following form:

$$4F_{\nu_x} = \frac{1}{4\pi R^2}[\cos^2(\theta_{12})\Phi_x + \sin^2(\theta_{12})\bar{\Phi}_e + \Phi_e + 2\Phi_x] \quad (2.25)$$

The equation now completely resembles equation 2.8. For inverted hierarchy, one can now see that $p_{ee} = \sin^2(\theta_{12})$ and $\bar{p}_{ee} = 0$. From here, the derivation for inverted hierarchy follows exactly as the above:

Inverted Hierarchy

$$F_e(R) = \frac{1}{4\pi R^2}[\sin^2(\theta_{12})\Phi_e(R_\nu) + \cos^2(\theta_{12})\Phi_x(R_\nu)] \quad (2.26)$$

$$F_\mu(R) + F_\tau(R) = \frac{1}{4\pi R^2}[\cos^2(\theta_{12})\Phi_e(R_\nu) + \Phi_x(R_\nu) + \sin^2(\theta_{12}\Phi_x(R_\nu))] \quad (2.27)$$

$$\bar{F}_e(R) = \frac{1}{4\pi R^2}[\bar{\Phi}_x(R_\nu)] \quad (2.28)$$

$$\bar{F}_\mu(R) + \bar{F}_\tau(R) = \frac{1}{4\pi R^2}[\bar{\Phi}_e(R_\nu) + \bar{\Phi}_x(R_\nu) + \sin^2(\theta_{12})\bar{\Phi}_x(R_\nu)] \quad (2.29)$$

We have now described how a neutrino can oscillate via MSW effects at low resonance. We first choose a method of interpolation to effectively "fill in the gaps" on the new energy grid required by the SG software package, interpolate the CHIMERA data and then perform the necessary calculations to describe how each flavor oscillates in vacuum. This process creates a new set of data files for 2D and 3D simulations that are then fed into SNOwGLoBES so that realistic neutrinos signatures can be generated for each of the provided detector configurations. Our final task is to produce meaningful plots that should agree with what the equations tell us about neutrino oscillation.

Chapter 3

Results

3.1 2D vs. 3D

The difference between the hydrodynamic flows in Chimera simulations in 2D and 3D can be best understood visually. Figure 3.1, provides images of the entropy for several time slices. Comparing these, the reader would notice a significant in-fall of material onto the PNS in the 2D along the equator. In 3D, we do not see such a single large scale in-fall of material. Instead, the material is falling toward the PNS along the margins of a number of up-flows, changing in time, but overall accretion occurs at a relatively constant rate. Although there are a plethora of other differences between the two types of simulations, this particular one has a direct impact on the neutrino luminosities. Figures 3.2, 3.3, 3.4 and 3.5 show each neutrino flavor number luminosity as a function of time, illustrating how the aforementioned differences in accretion behavior affects the data output from Chimera. In 2D, we see a very "noisy" plot, especially beyond 150 ms. These jagged points along the plots are where significant variations in the amounts of material falling onto the PNS as if someone was hammering material into the PNS. In 3D, we see the luminosities are smoothed out considerably, agreeing with more constant falling of material on the PNS (e.g. the soft, constant pouring of rain).

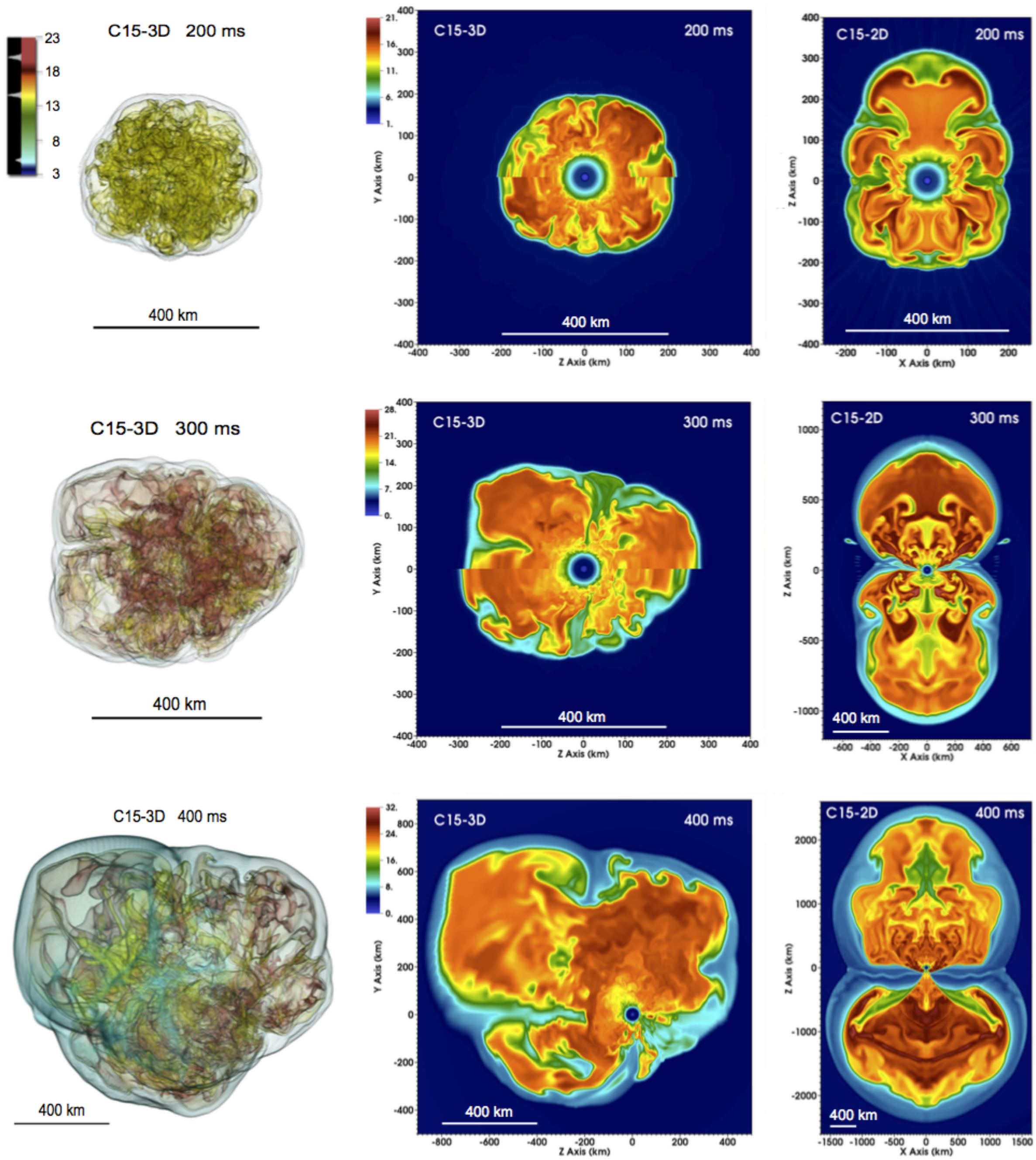

Figure 3.1: Difference in 2D and 3D (from Lentz et al. (2015))

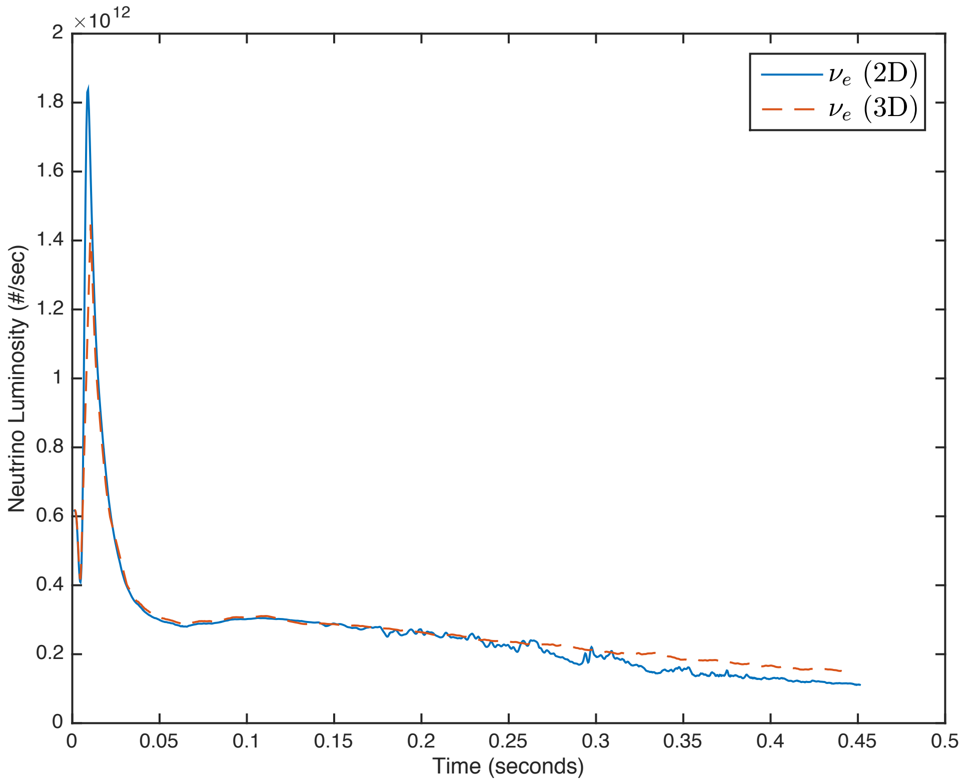

Figure 3.2: Number Luminosity vs. time for ν_e

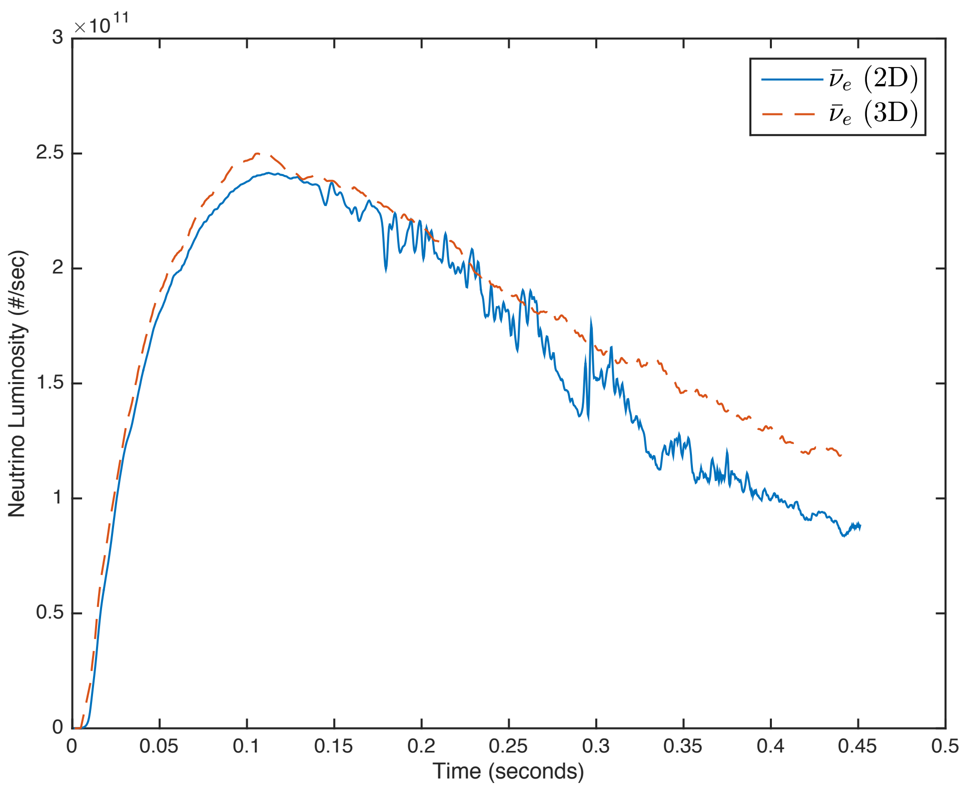

Figure 3.3: Number Luminosity vs. time for $\bar{\nu}_e$

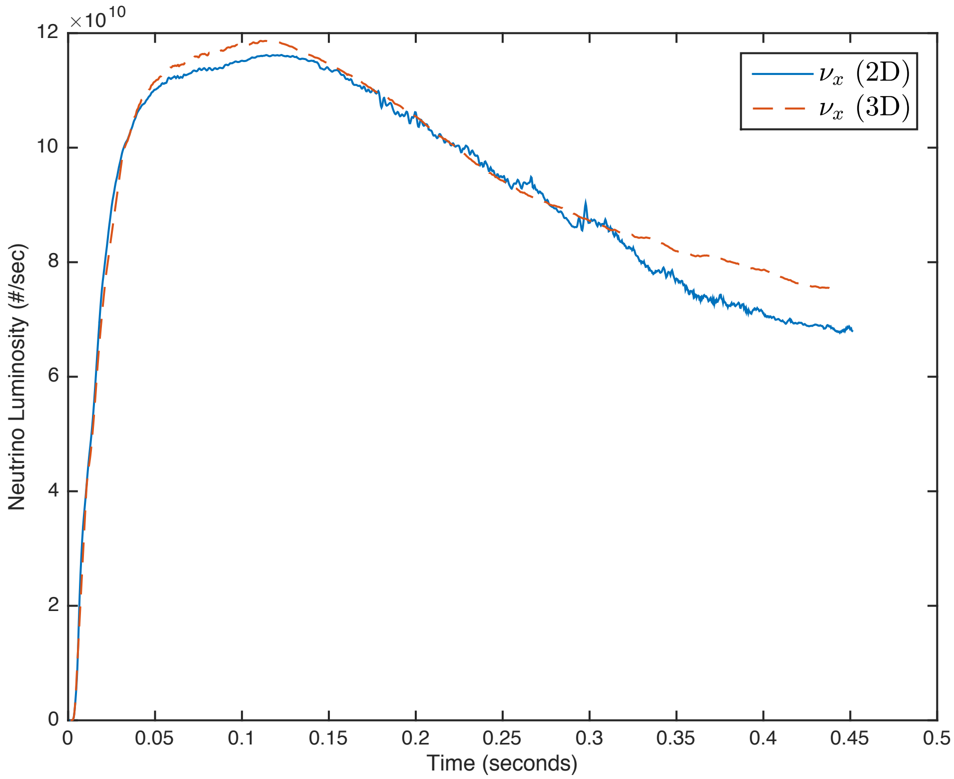

Figure 3.4: Number Luminosity vs. time for ν_x

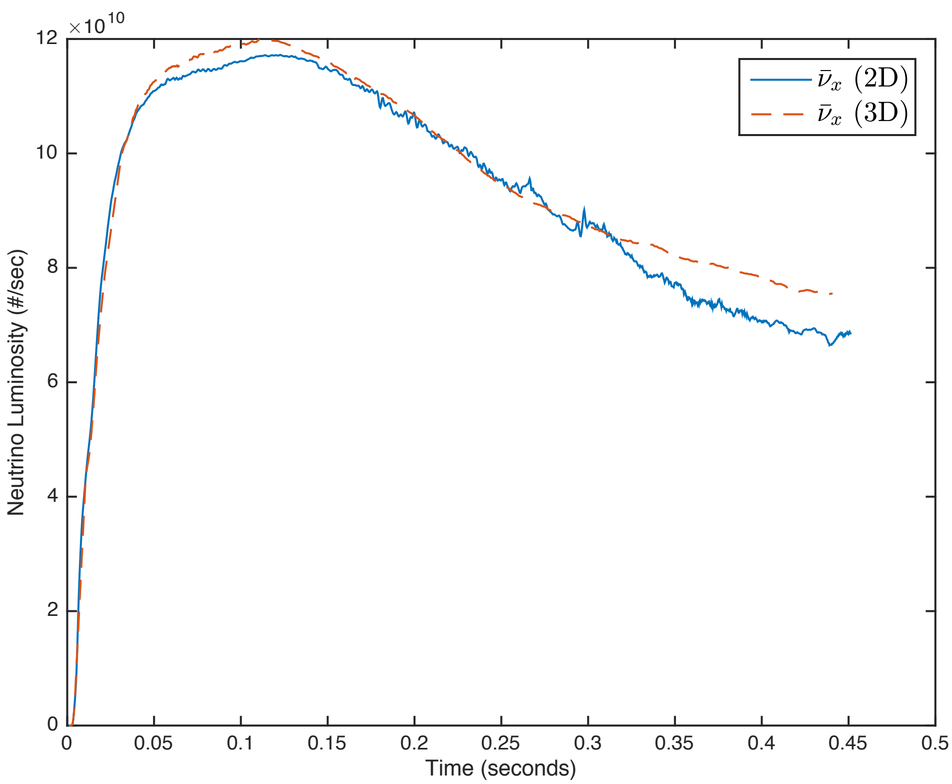

Figure 3.5: Number Luminosity vs. time for $\bar{\nu}_x$

3.2 Oscillation Behavior

For the normal hierarchy, we expect all of the ν_e neutrinos to oscillate completely to the ν_x flavor in vacuum as a prime example. It is important to note that because ν_x represents the summation of ν_μ and ν_τ, we can only say ν_e oscillates to ν_μ or ν_τ. We cannot differentiate to which ν_e oscillates precisely. To visualize this, illustrate the total number of neutrinos versus energy (Figures 3.6 and 3.7). These figures are of 2D - Normal Hierarchy simulations only. Equivalent results are obtained when viewing 3D data. Taking into account equations 2.20-2.23, we should notice several lines change position on the plot when vacuum oscillations are considered (indicated by dashed lines). The most evident change is ν_e, which oscillates to exactly half of the ν_x flavor represented by the black solid and dashed lines. Figures 3.8 and 3.9 illustrate the equivalent prediction for inverted hierarchy; $\bar{\nu}_e$ oscillates to half of the $\bar{\nu}_x$ flavor. These time-summed plots were used as a check that the calculations in our code behaved correctly. These plots confirmed we were performing the calculations as laid out in chapter 2 accurately.

Figures 3.10 and 3.11 display the neutrino luminosity versus time for a 2D, angle averaged simulation of a supernova using the Chimera code. Included with this plot are predictions for how the neutrino flavors oscillate as in the preceding figures for normal and inverted hierarchy. Again, figure 3.10 demonstrates that each flavor of neutrino oscillates as anticipated in Equations 2.20-2.23 (normal hierarchy). Again, the dashed black line denotes the oscillation of ν_e to half of the ν_x flavor of neutrino completely. Note, that while Chimera simulations distinguish between ν_x and $\bar{\nu}_x$, their luminosities effectively have the same value, thus, the two flavors occupy the same line with no oscillation (solid line) in the figure. Equivalent results were obtained for 3D simulations. Figures 3.6 - 3.11 were taken at $\sim$450 ms post-bounce.

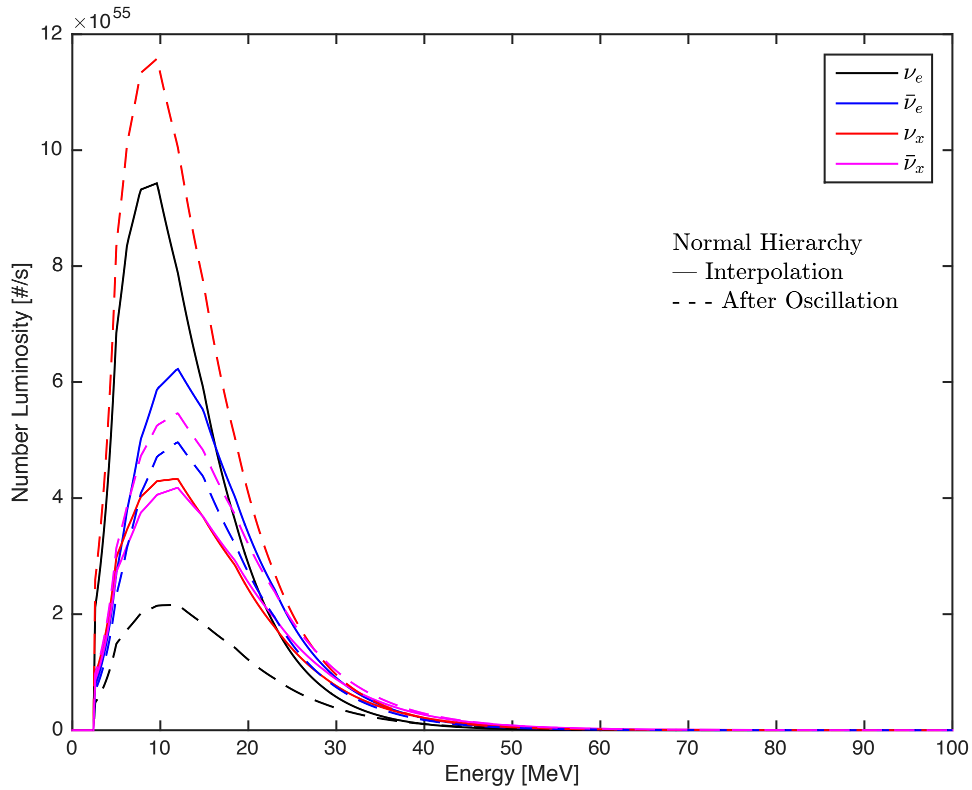

Figure 3.6: Neutrino Flavor Oscillation - Normal Hierarchy in 2D

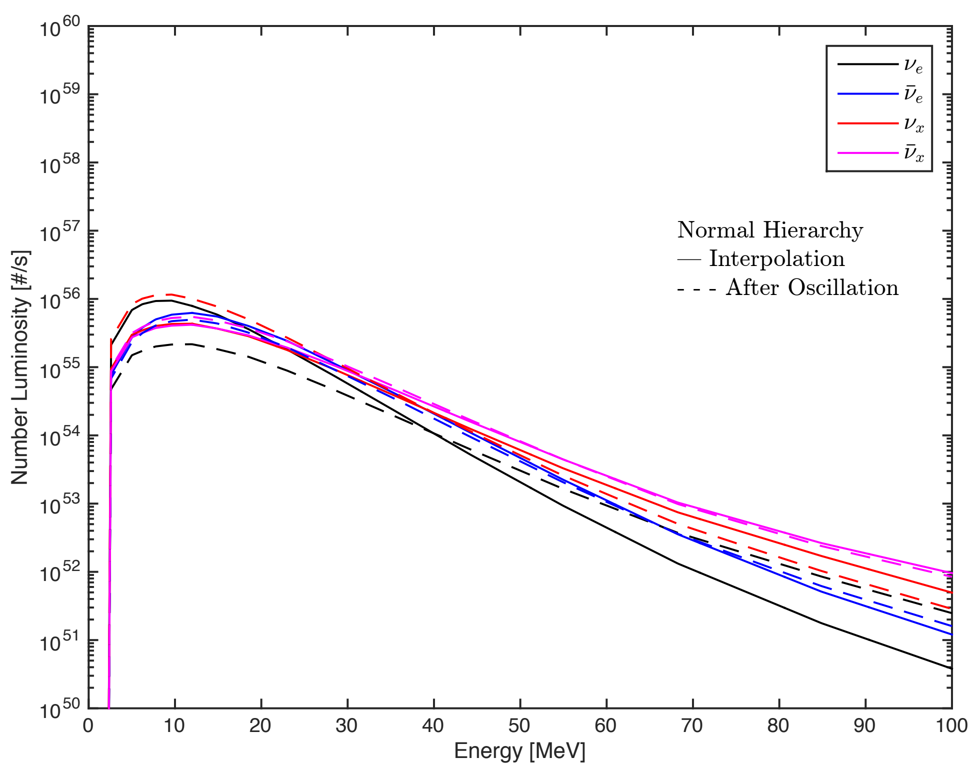

Figure 3.7: Normal Hierarchy - High Energy Tail in 2D

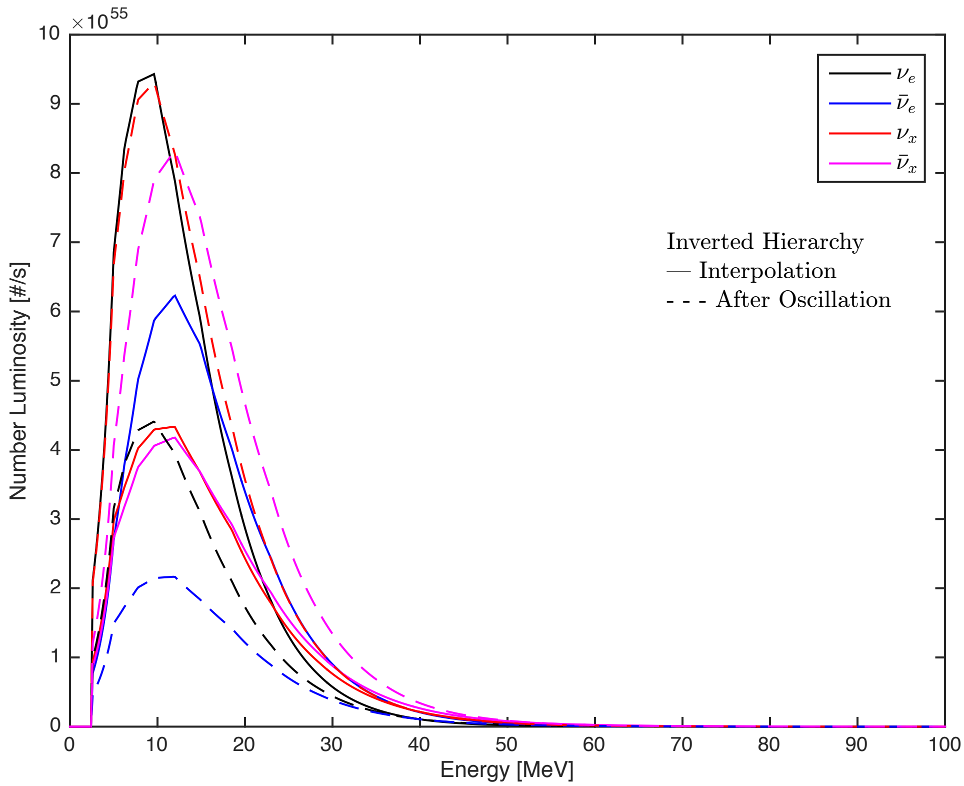

Figure 3.8: Neutrino Flavor Oscillation - Inverted Hierarchy in 2D

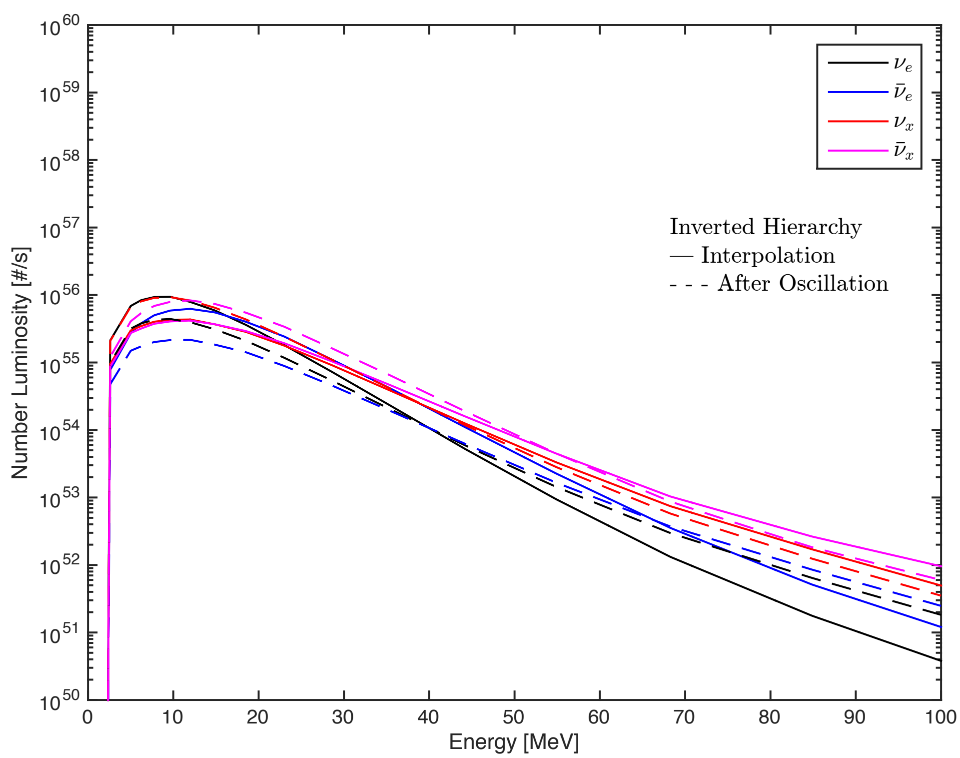

Figure 3.9: Inverted Hierarchy - High Energy Tail in 2D

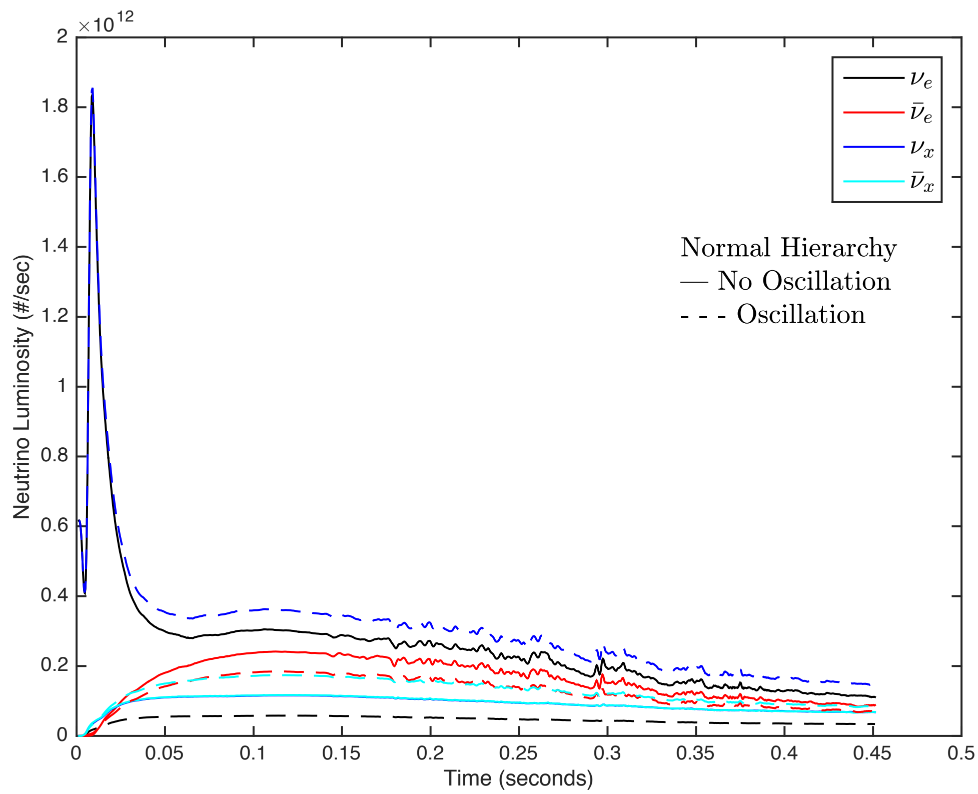

Figure 3.10: Number Luminosity vs. Time - Normal Hierarchy in 2D

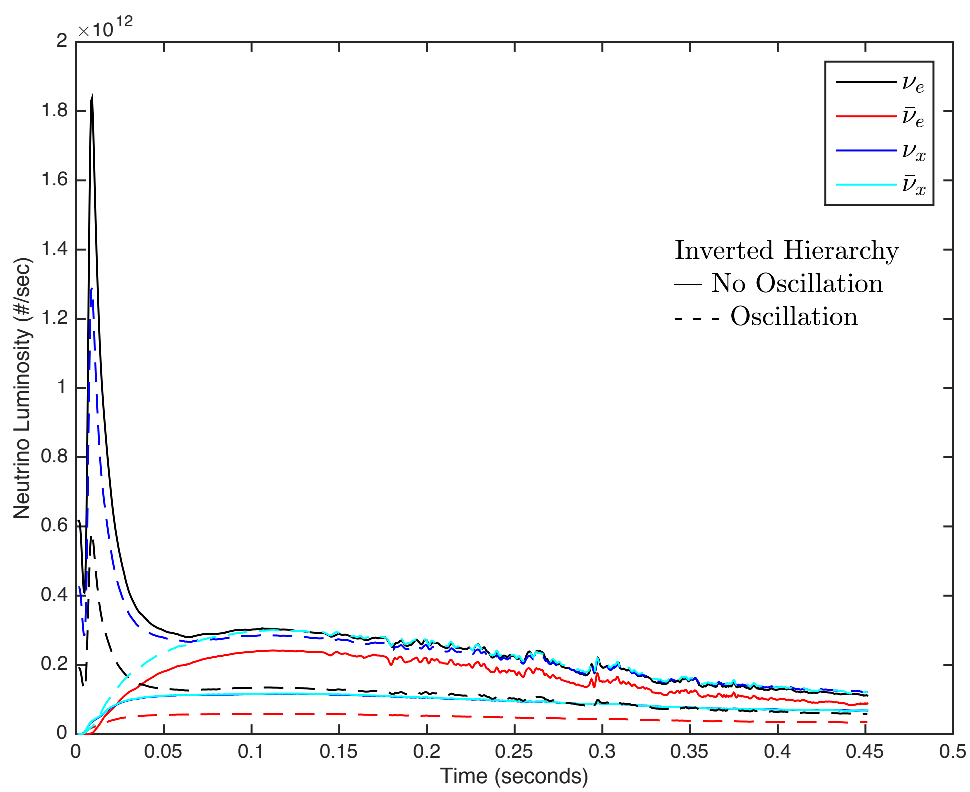

Figure 3.11: Number Luminosity vs. Time - Inverted Hierarchy in 2D

3.3 SNOwGLoBES

The final step is to pass the Chimera neutrino signals, modified by the oscillations into the simulated detectors of the SNOwGLoBES software package. This will tell us how the total number of neutrinos detected behaves as a function of time and therefore what a terrestrial neutrino detector might find if a supernova were to happen in the Galaxy.

Figures 3.12 through 3.19 display information about the total number of neutrinos detected as a function of time for 2D and 3D as well as for normal and inverted hierarchy. For each plot, we only include the dominant detection channels for each type of detector (argon, lead, scintillator and water). The first notable trend is that we see more overall neutrinos in 3D than we do in 2D. This is still being investigated, but the current consensus is that, in 3D simulations with Chimera, the explosion develops more slowly, allowing accretion to continue and the the proto-neutron star (PNS) has slightly higher mass than in 2D. This would lead to an increase in neutrino production across the board in the event of a supernova. Investigating the counts for Argon, we see the expected burst of neutrinos at ∼0.025 seconds. This, of course corresponds to the PNS becoming transparent to neutrinos thus, releasing the trapped ν_e neutrinos. After vacuum oscillations, ν_e has oscillated to half of ν_x. This is illustrated by the solid black line displaying a more constant count of neutrinos over time. This is due to the ν_x neutrino sphere being located further within the PNS as explained in Chapter 2.

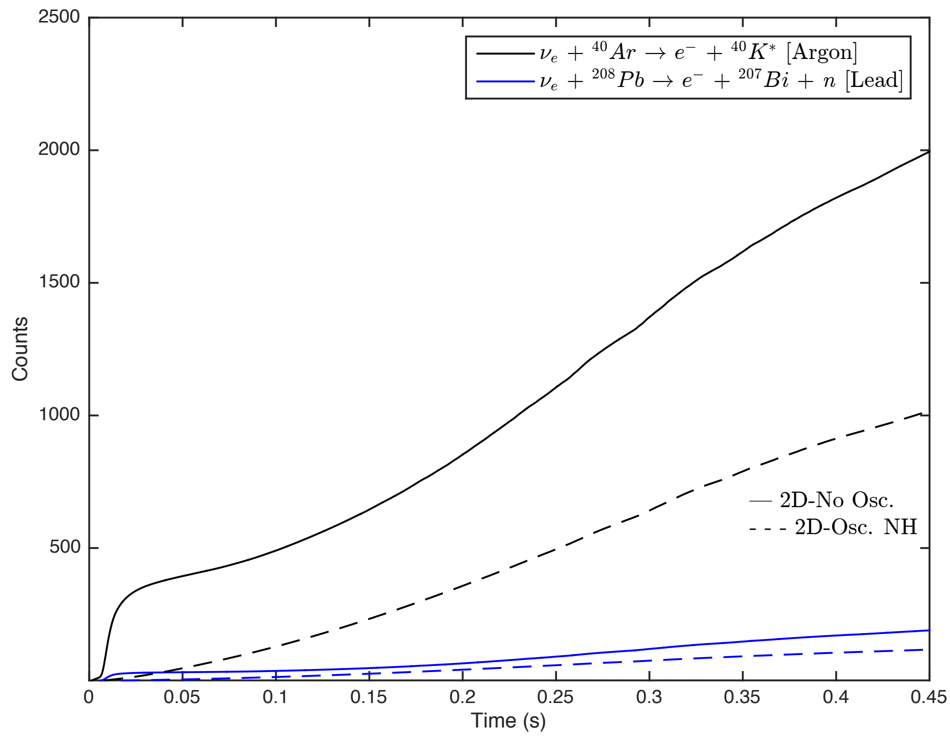

Figure 3.12: Total Count vs. Time (Argon & Lead Interactions in 2D - NH)

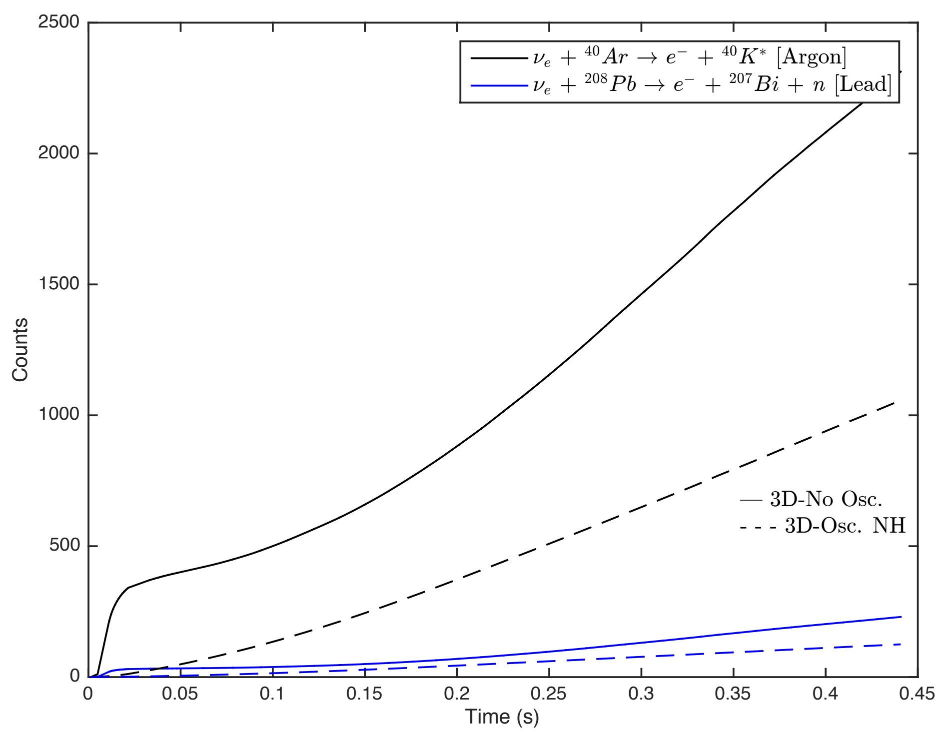

Figure 3.13: Total Count vs. Time (Argon & Lead Interactions in 3D - NH)

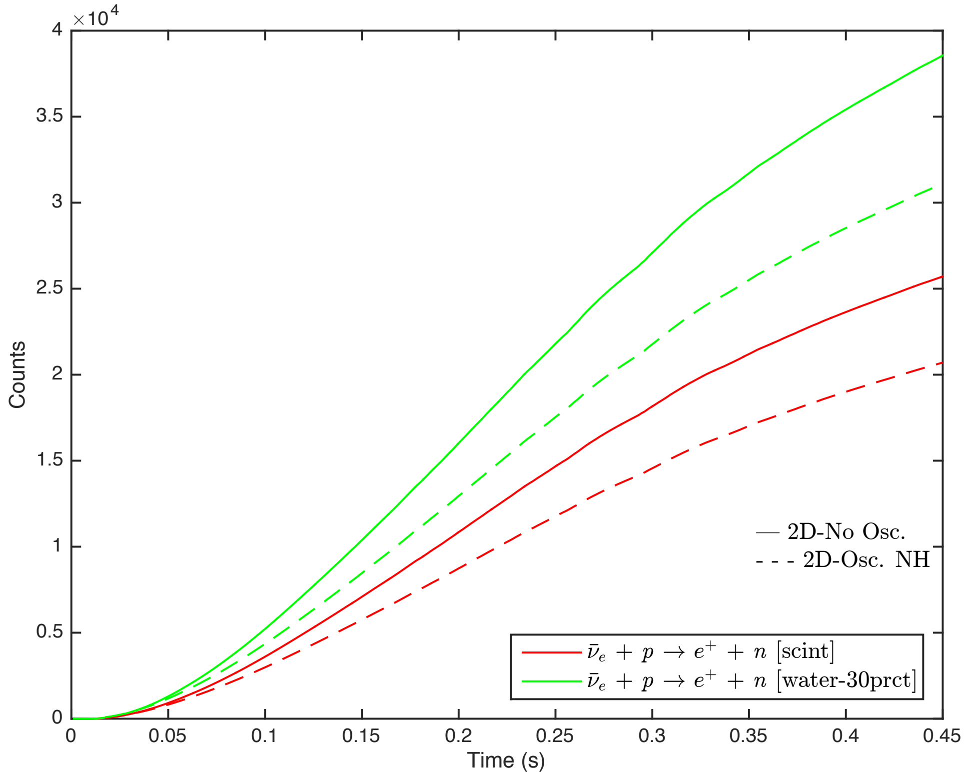

Figure 3.14: Total Count vs. Time (Inverse Beta Decay in 2D - NH)

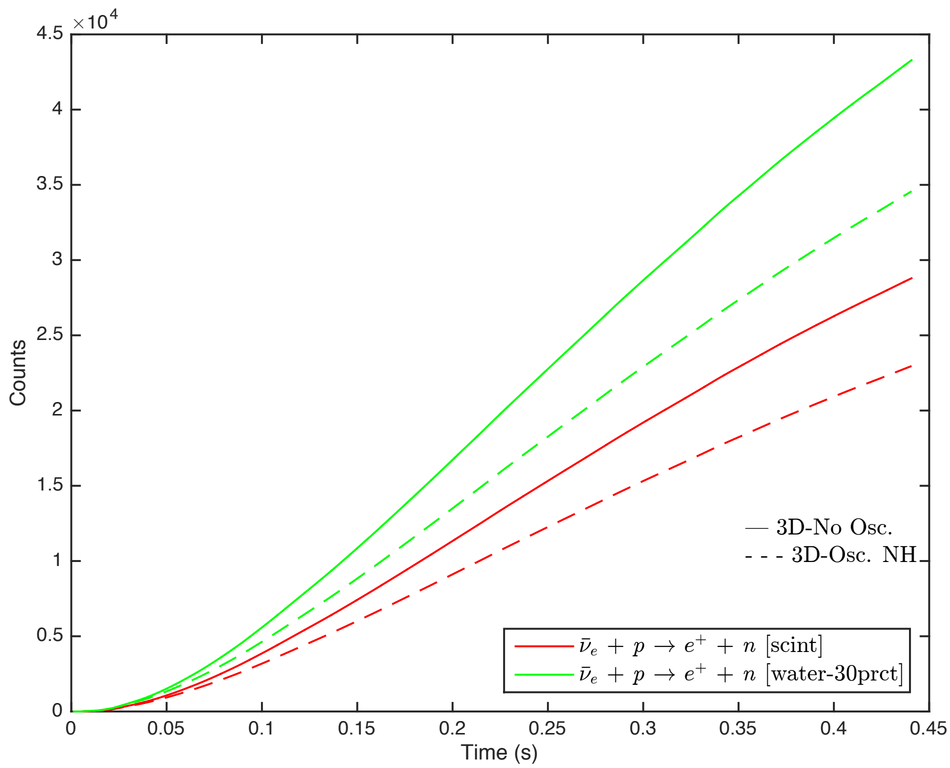

Figure 3.15: Total Count vs. Time (Inverse Beta Decay in 3D - NH)

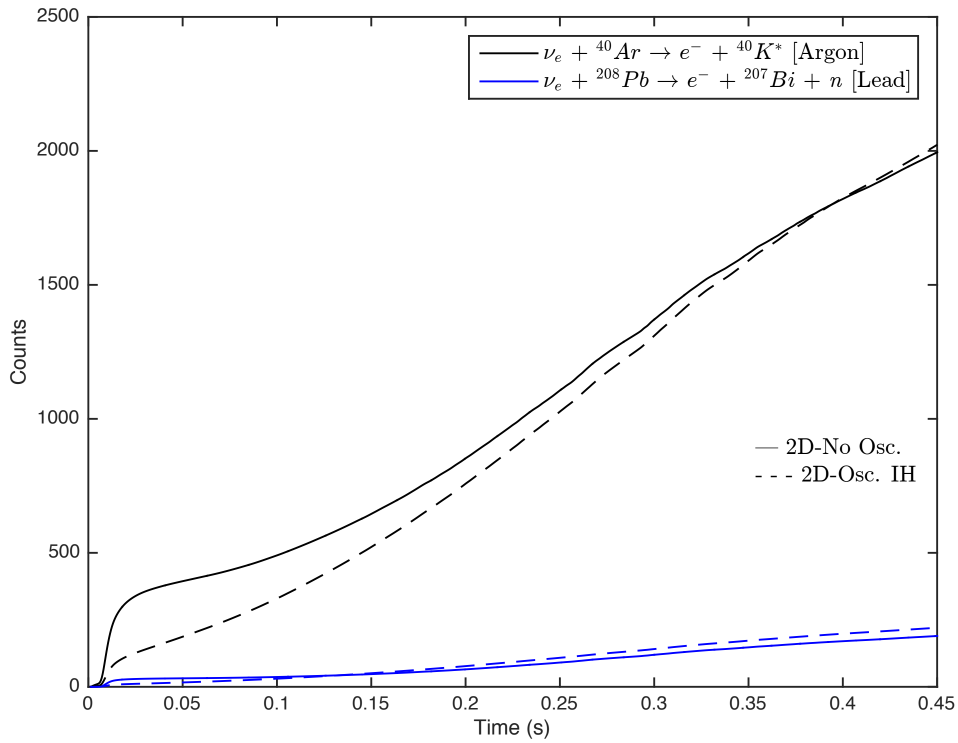

Figure 3.16: Total Count vs. Time (Argon & Lead Interactions in 2D - IH)

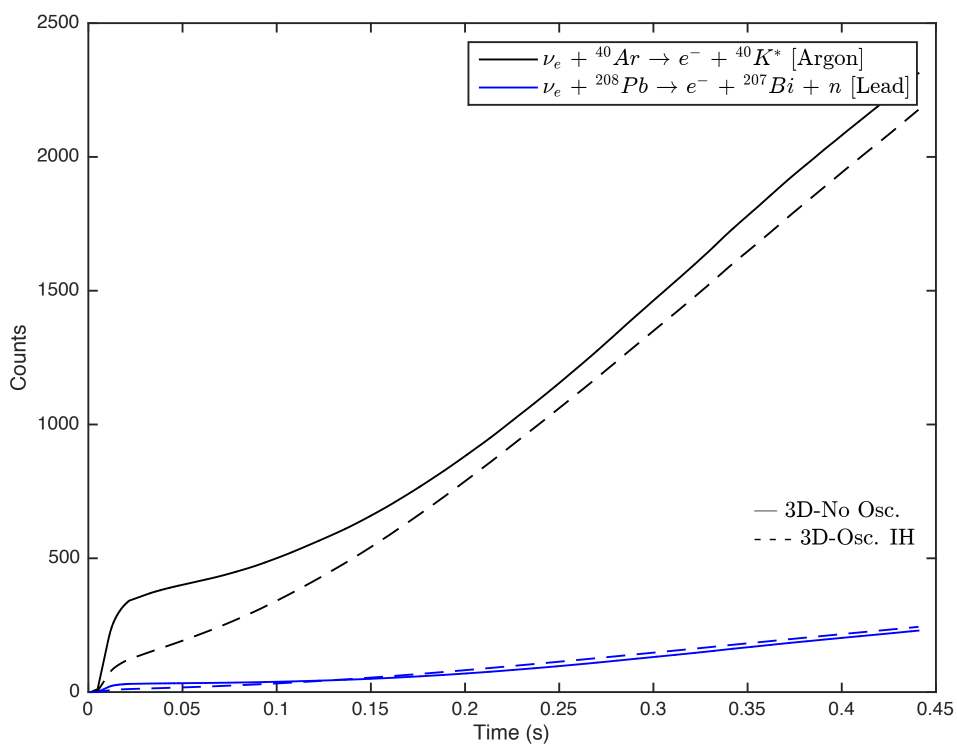

Figure 3.17: Total Count vs. Time (Argon & Lead Interactions in 3D - IH)

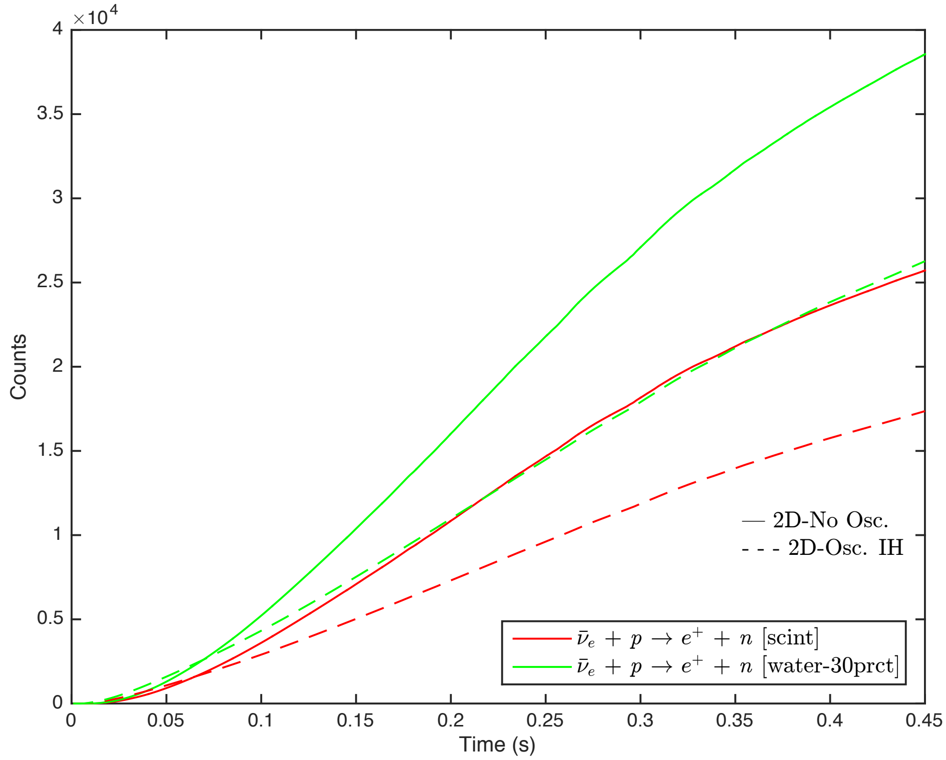

Figure 3.18: Total Count vs. Time (Inverse Beta Decay in 2D - IH)

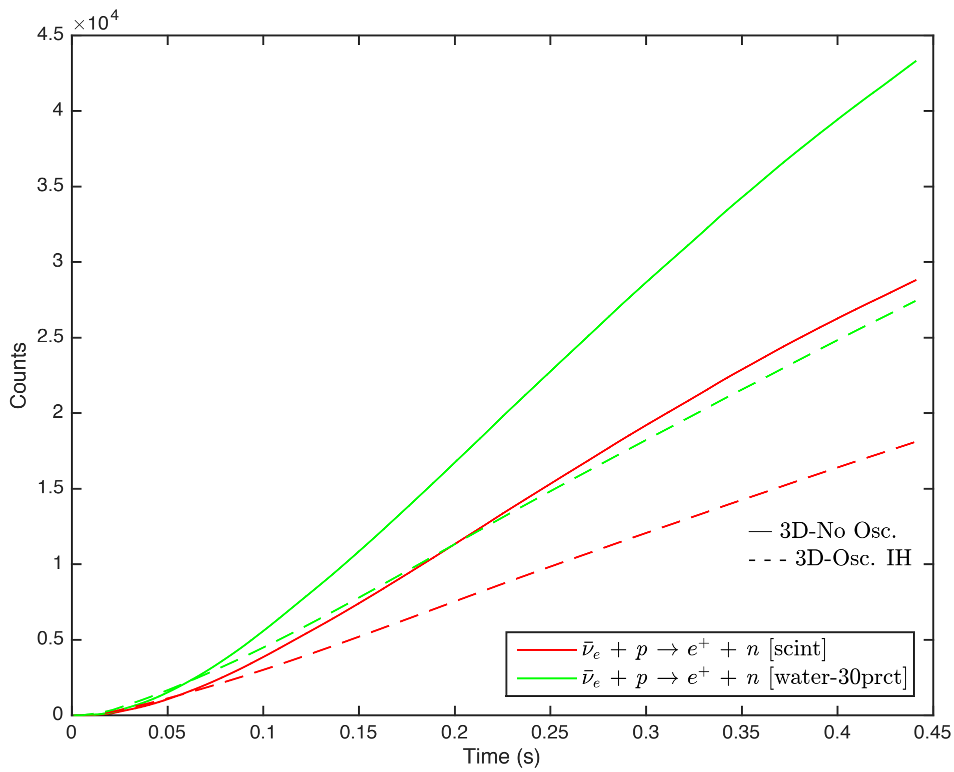

Figure 3.19: Total Count vs. Time (Inverse Beta Decay in 3D - IH)

Figures 3.20 and 3.23 display the spectral output (counts per 0.5 MeV) for the dominant channels corresponding to the aforementioned detectors. The counts are situated on an energy grid separated by a 0.5 MeV for each step. The solid lines represent no oscillations while the dashed lines include low resonance MSE effects (normal and inverted included). As one can see, low resonance MSW effects cause the overall peak to shift, in the case of Argon and Lead detectors, or decrease in the case of inverse beta decay. Moreover, it is quite evident that the high energy tail of each flavor spectrum is significantly boosted (indicating a "harder" spectra). We will discuss this further in the context of an individual detector shortly. Figures 3.24 and 3.25 compare normal and inverted hierarchy oscillation schemes in 2D and 3D simulations. Figures 3.20 - 3.25 were taken at ∼450 ms post-bounce.

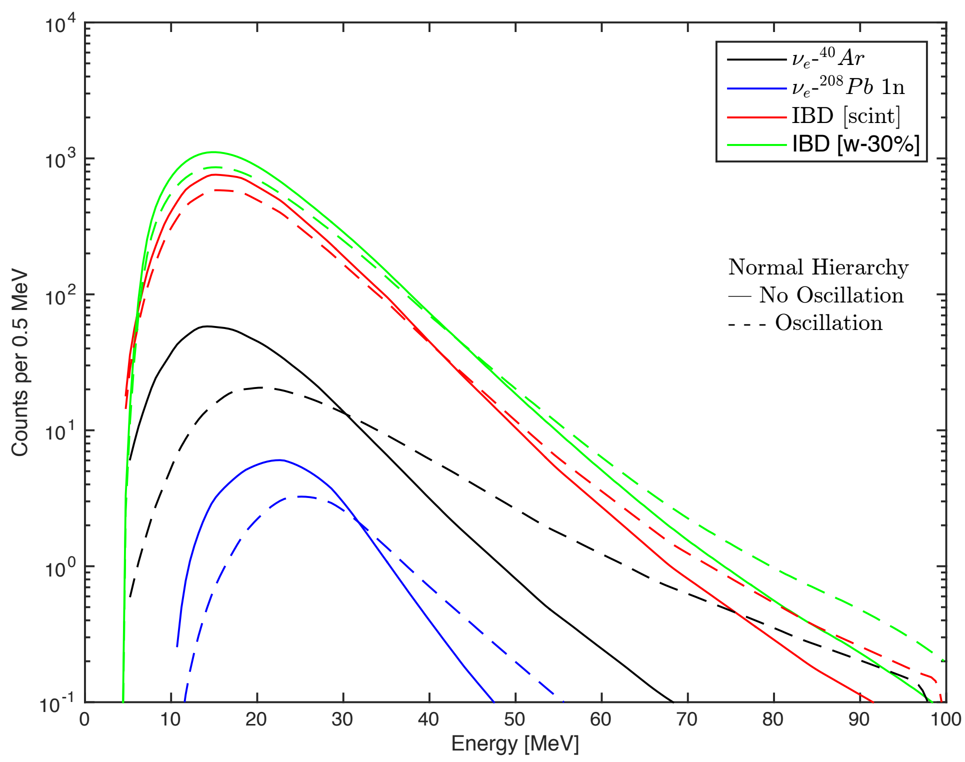

Figure 3.20: Dominant Channels - Normal Hierarchy in 2D

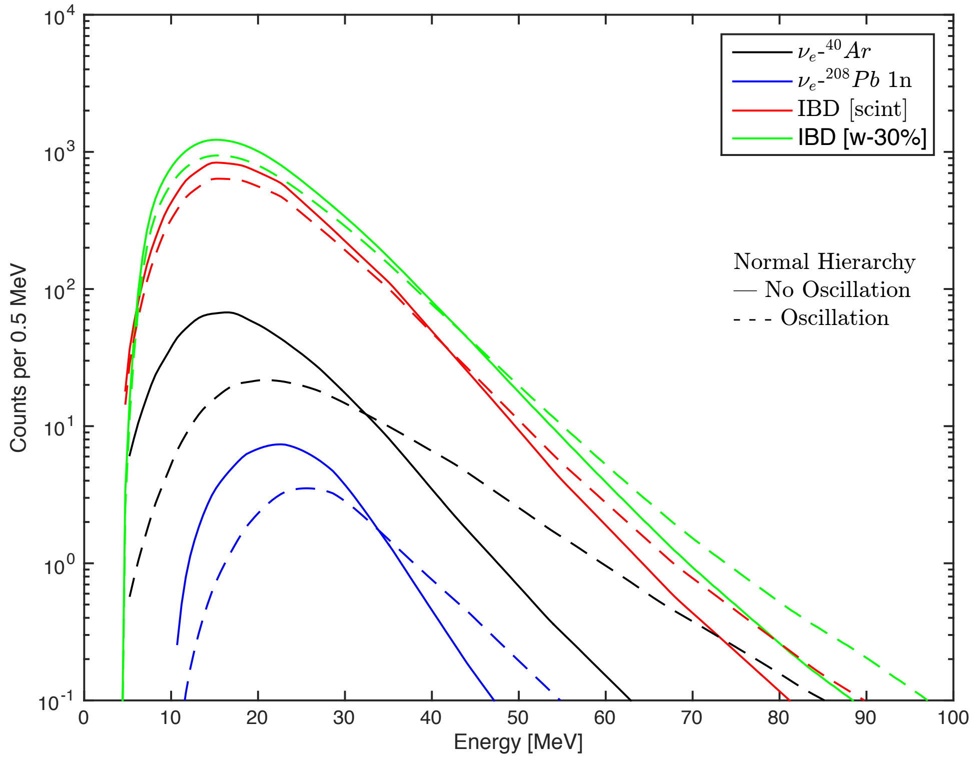

Figure 3.21: Dominant Channels - Normal Hierarchy in 3D

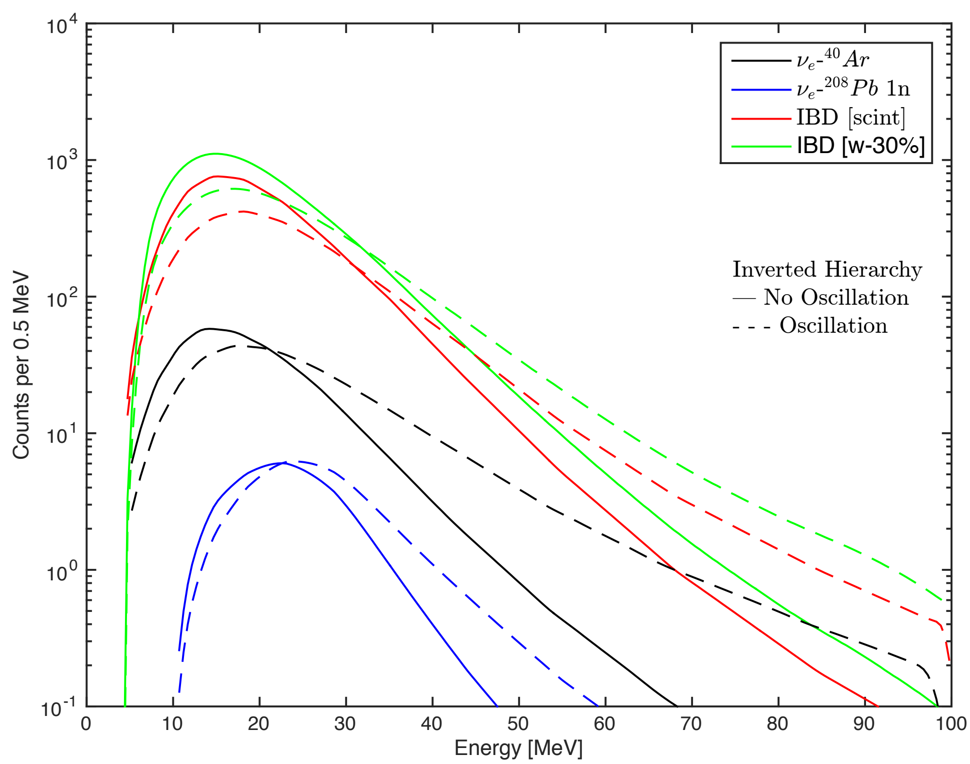

Figure 3.22: Dominant Channels - Inverted Hierarchy in 2D

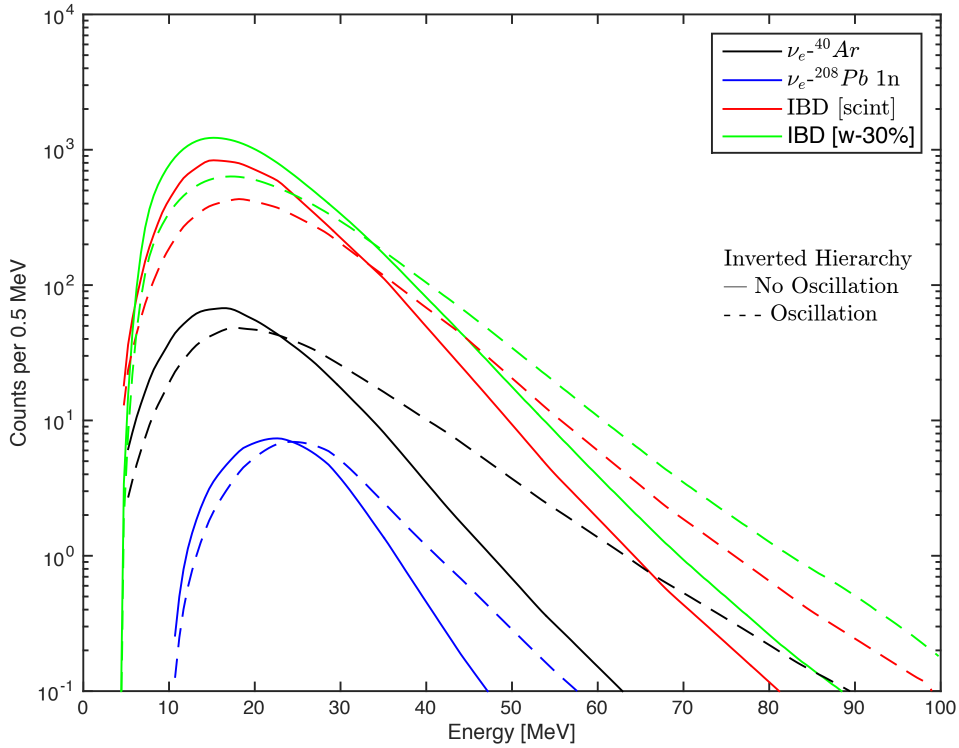

Figure 3.23: Dominant Channels - Inverted Hierarchy in 3D

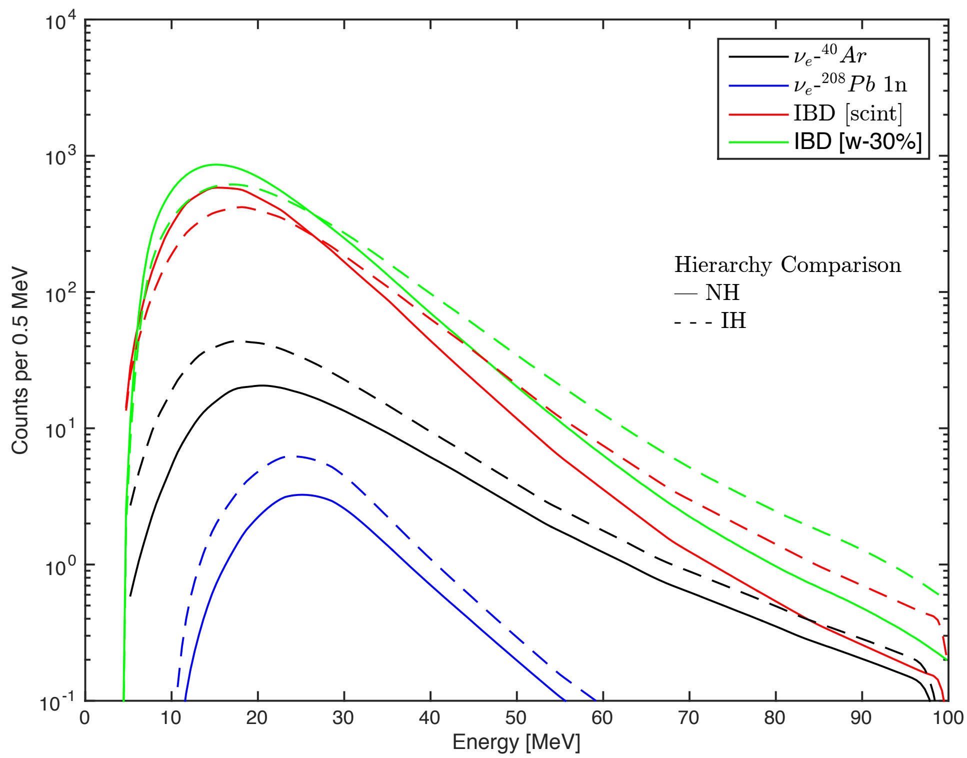

Figure 3.24: Dominant Channels - Hierarchy Comparison in 2D

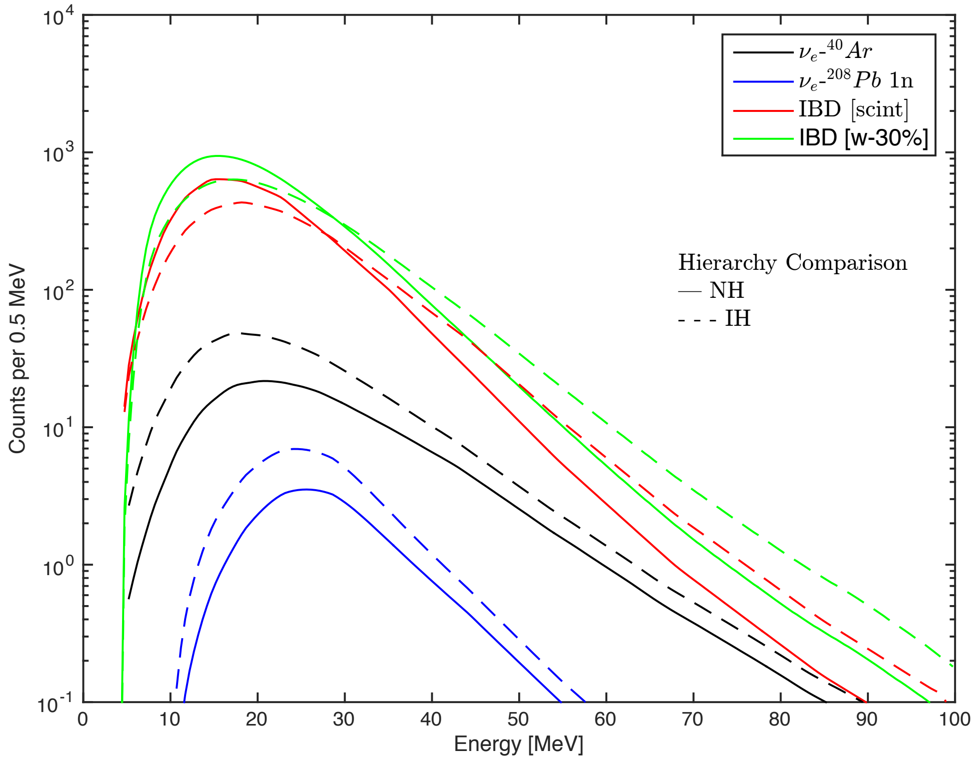

Figure 3.25: Dominant Channels - Hierarchy Comparison in 3D

Figures 3.26 through 3.33 display the the detection channels available to an argon detector for 2D and 3D simulations as well as for normal and inverted hierarchy. We highlight Argon because it is the only material that differentiates between all flavors of neutrino, most importantly ν_e and $\bar{\nu}_e$. We use it here to illustrate how low resonance MSW effects affect the overall spectrum of neutrinos for each flavor. Examining Figures 3.26 and 3.27, we see that, for normal hierarchy, the spectra becomes "harder" when oscillations are included. This is most easily explained by examining the spectrum for charged-current interactions with ν_e, or the black solid and dashed lines. Recall that for normal hierarchy, ν_e oscillates completely to half of the ν_x flavor in vacuum. Thus, ν_e neutrinos that reach the detector left the supernova as ν_x neutrinos and represent the harder spectra. Similar results are found by examining Figures 3.28 and 3.29 for inverted hierarchy. Figures 3.30 through 3.33 illustrate how ν_x, when oscillating to ν_e exhibits a "softer" spectrum. Figures

3.34 through 3.37 illustrate the difference between normal and inverted hierarchy oscillations.

Within the supernova, neutrinos decouple from matter at different distances from the center. For normal hierarchy, this means ν_e flavor neutrinos, having the highest opacity, decouple at a larger radius compared to the other flavors, while ν_x neutrinos decouple at a smaller radius where the temperature, and as a result the neutrino energy, are higher. This corresponds directly to what we see in the ν_e spectra for 2D and 3D simulations. The solid black line shows us a lower overall energy than that of the dashed black line. In other words, because ν_e oscillates completely to ν_x and ν_x oscillates to ν_e, we see the overall energy of ν_e go up and become a "harder" spectrum. Some of the remaining flavors also show a harder spectra while others soften (e.g. ν_x). All figures below were taken at ~450 ms post-bounce.

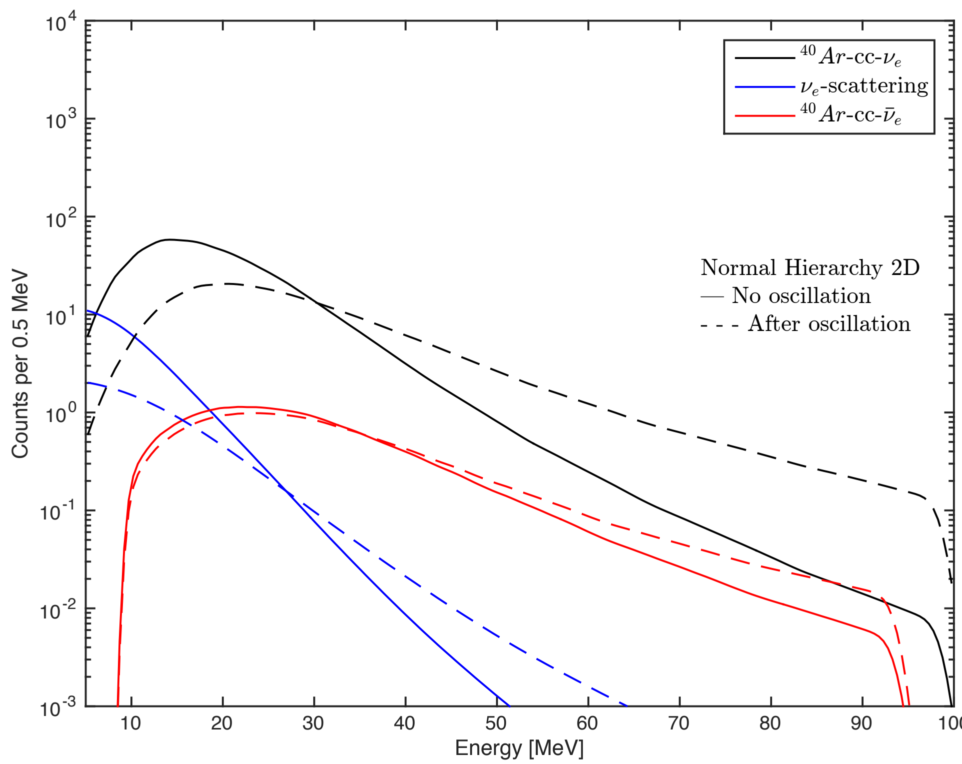

Figure 3.26: Detection Channels for Argon - Normal Hierarchy in 2D

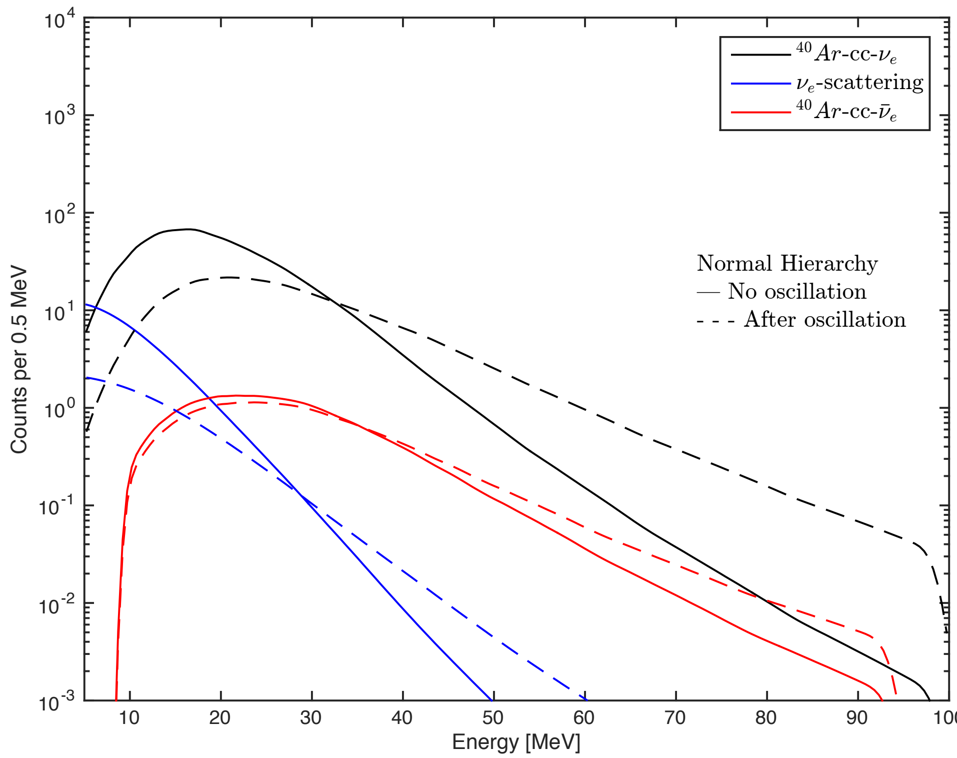

Figure 3.27: Detection Channels for Argon - Normal Hierarchy in 3D

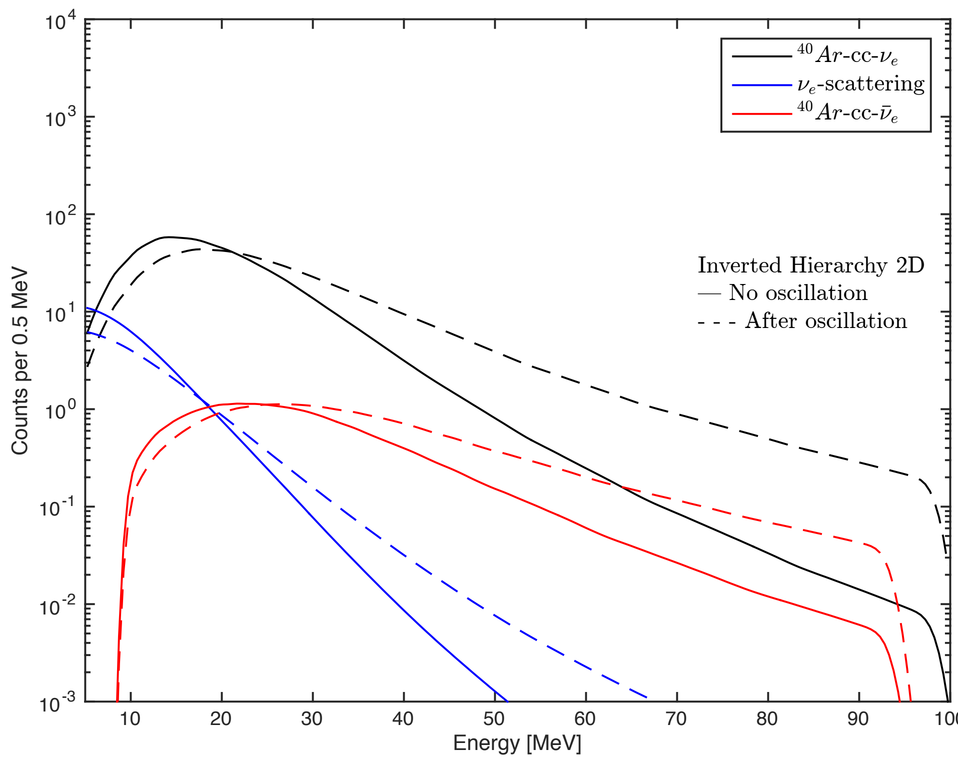

Figure 3.28: Detection Channels for Argon - Inverted Hierarchy in 2D

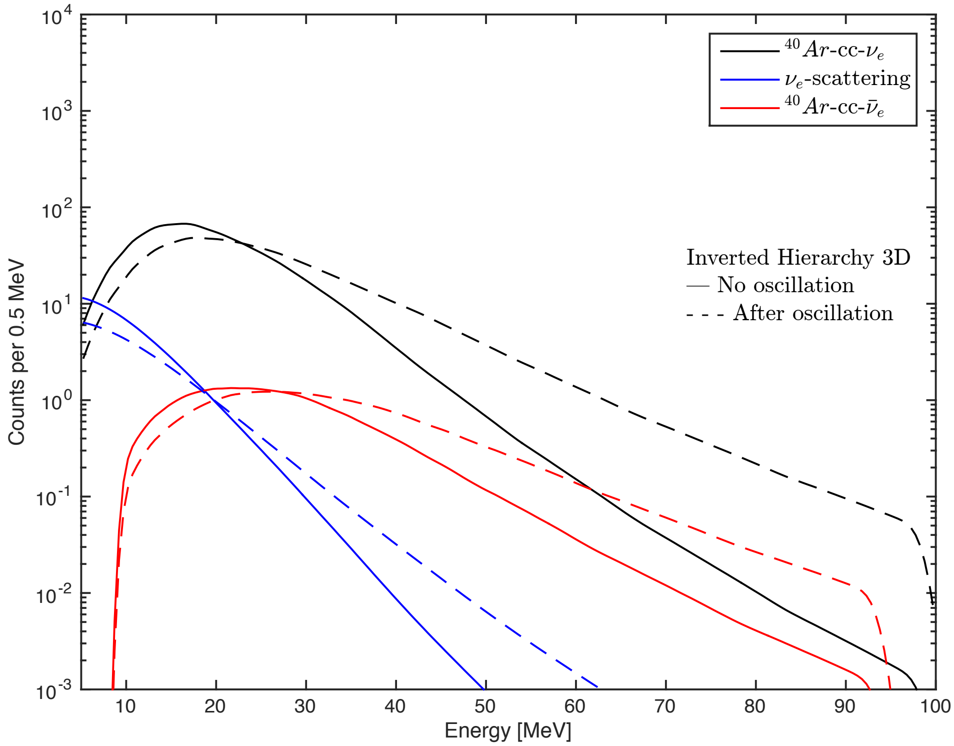

Figure 3.29: Detection Channels for Argon - Inverted Hierarchy in 3D

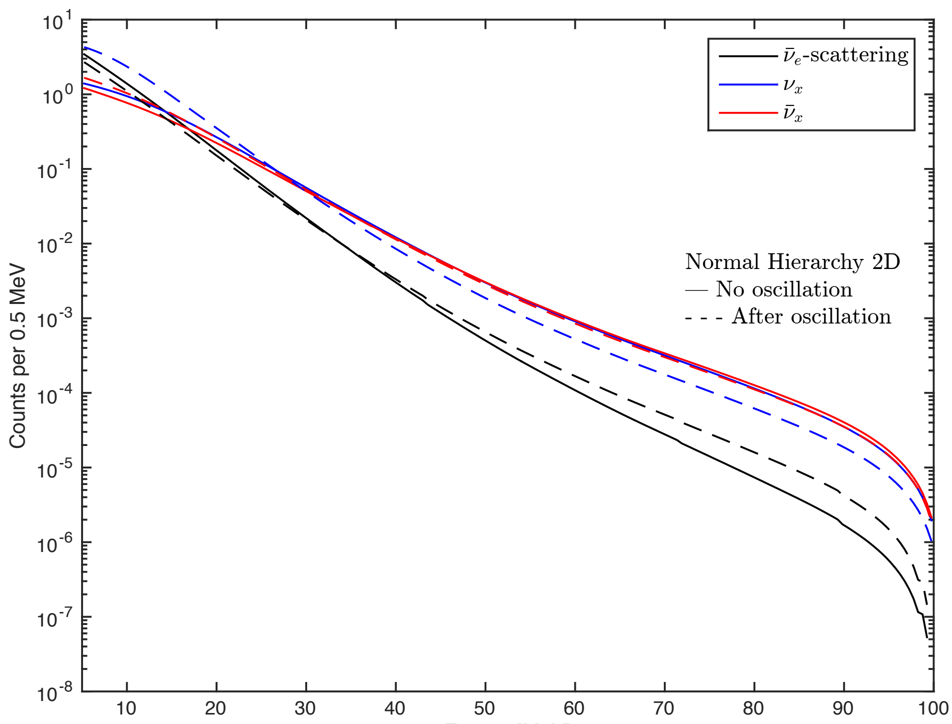

Figure 3.30: Detection Channels for Argon - Normal Hierarchy in 2D

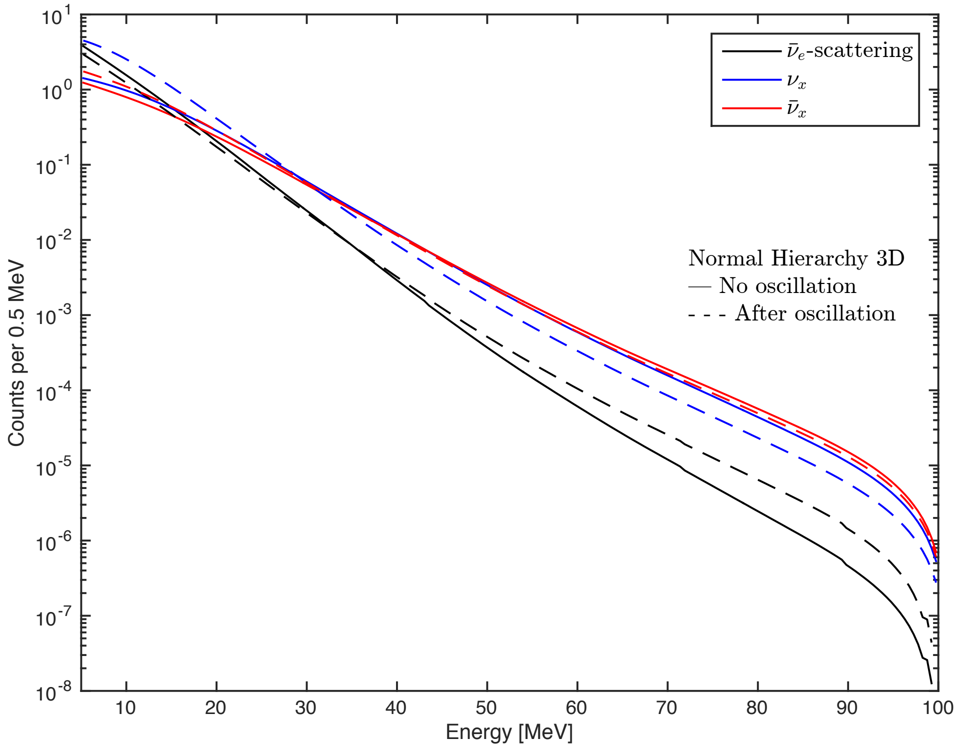

Figure 3.31: Detection Channels for Argon - Normal Hierarchy in 3D

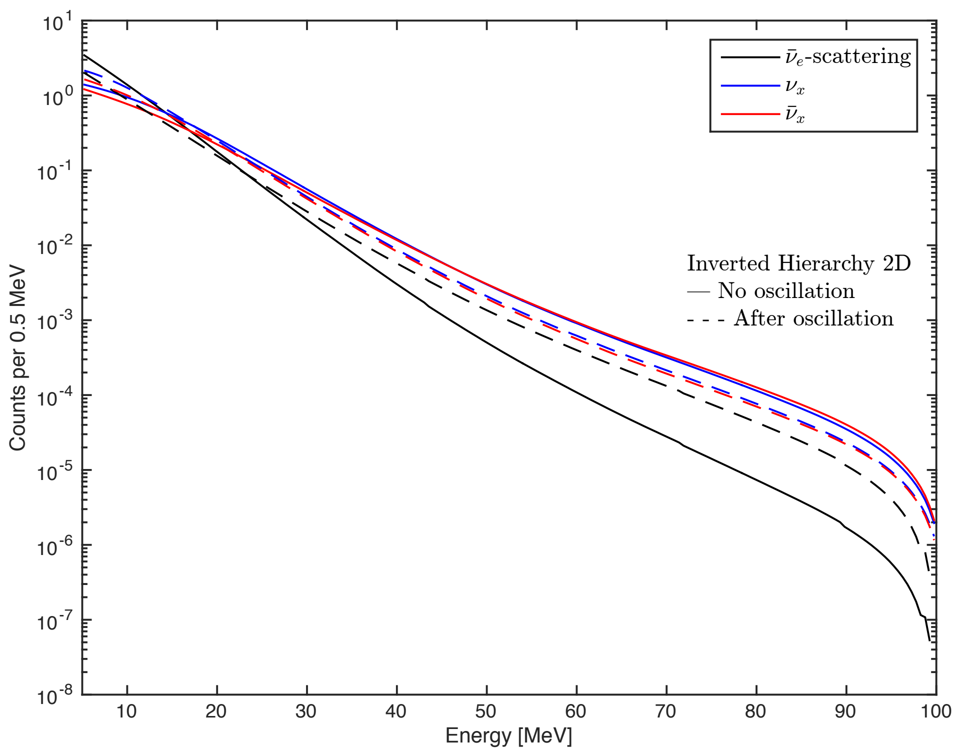

Figure 3.32: Detection Channels for Argon - Inverted Hierarchy in 2D

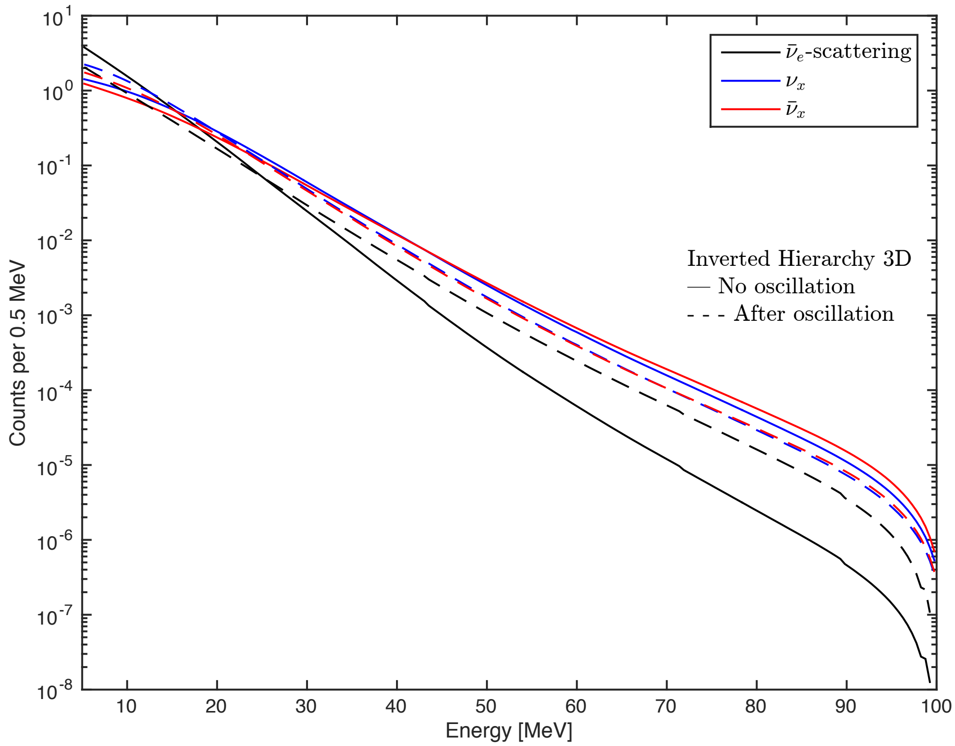

Figure 3.33: Detection Channels for Argon - Inverted Hierarchy in 3D

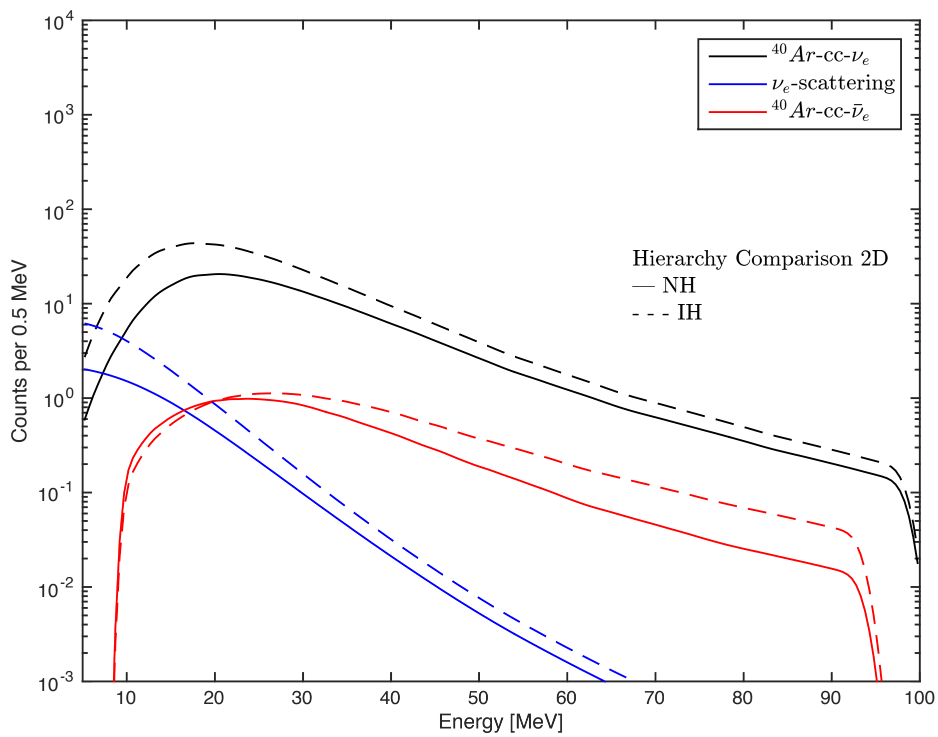

Figure 3.34: Detection Channels for Argon - Hierarchy Comparison in 2D

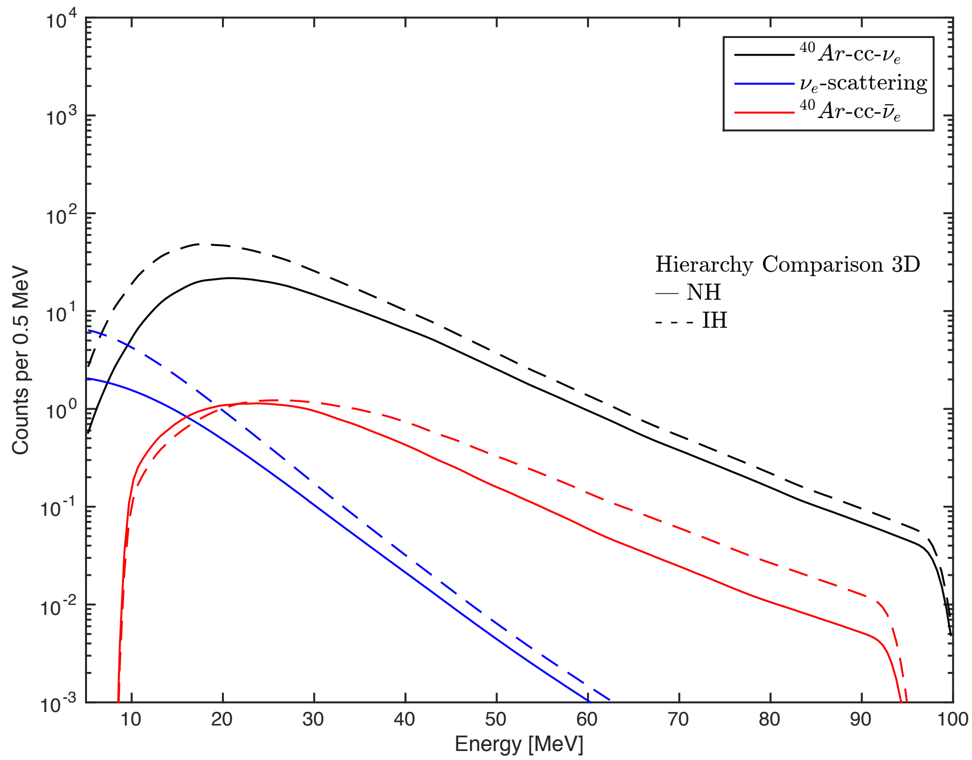

Figure 3.35: Detection Channels for Argon - Hierarchy Comparison in 3D

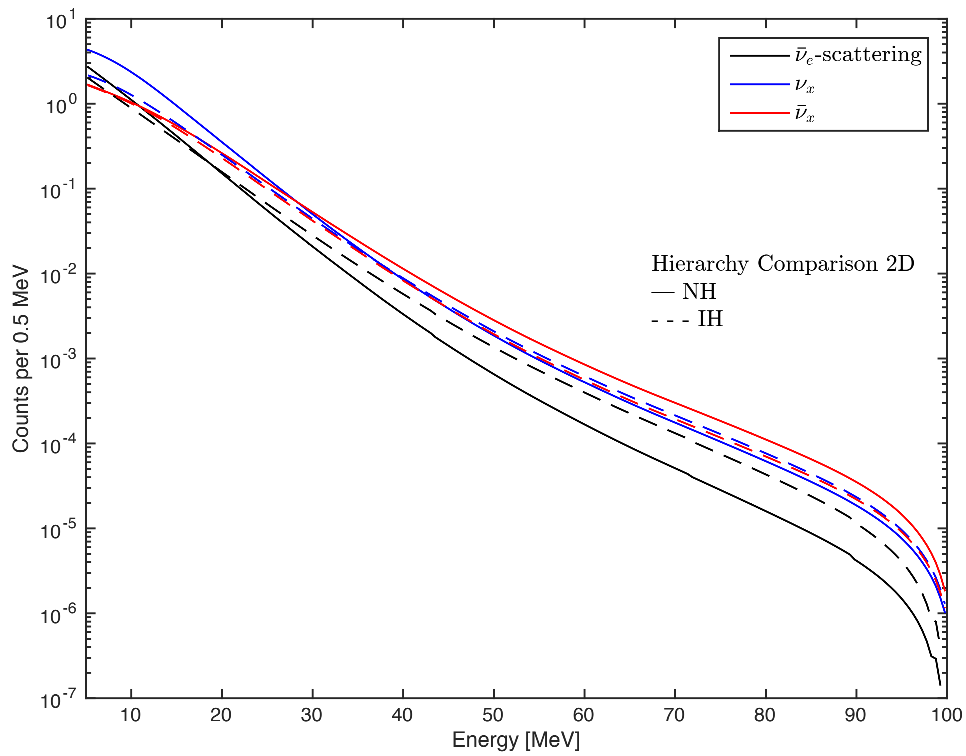

Figure 3.36: Detection Channels for Argon - Hierarchy Comparison in 2D

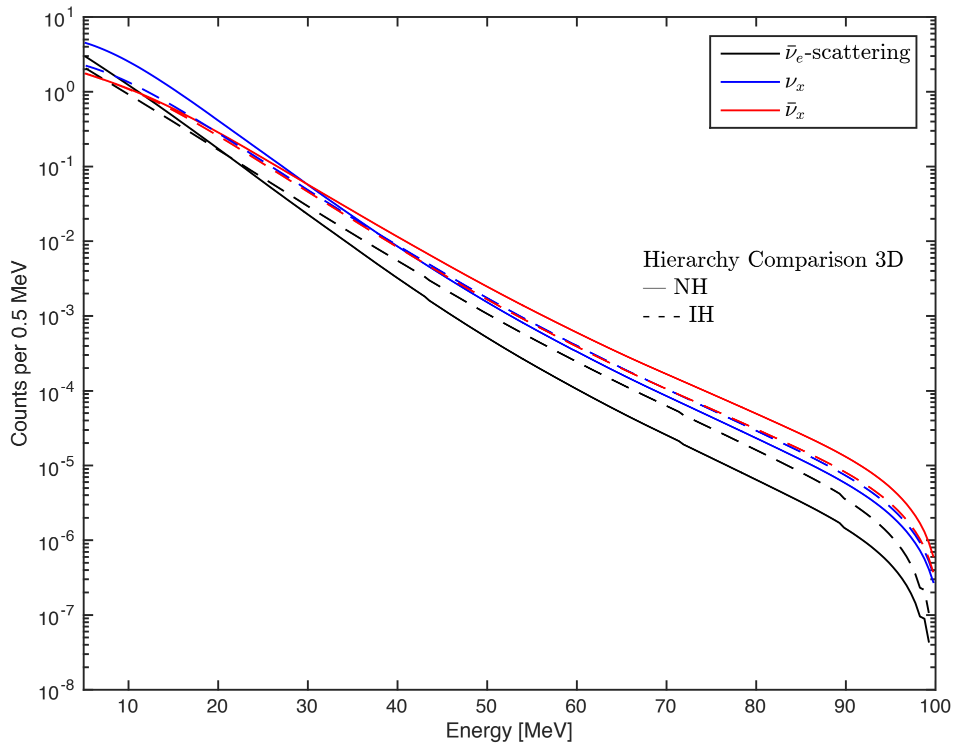

Figure 3.37: Detection Channels for Argon - Hierarchy Comparison in 3D

Chapter 4

Conclusions

In the broadest sense, we have investigated the neutrino signatures that originate from a star undergoing a supernova explosion. This investigation utilized data from the Chimera code (Lentz et al., 2015) which performed advanced supernova simulations in both two- and three-dimensions. Along with this, the software package SNOwGLoBES (Beck et al., 2013) was also utilized to perform an in depth analysis on the Chimera data to produce neutrino signatures consistent with detector configurations found on Earth. This gave a very detailed picture of what an Earth-based detector should find during a supernova. The neutrino signatures obtained from SNOwGLoBES are an invaluable insight into the inner mechanisms that play out during a supernova event. Furthermore, the consideration of low resonance MSW effects help further our understanding of what happens to neutrinos as they travel their path from the supernova to our terrestrial detectors. Through this work, we have helped to further our understanding of how neutrinos behave during a supernova and shown that this is a valuable exercise in testing our simulations through the data they produce.

While this work afforded us a new view of Chimera models through the eyes of terrestrial neutrino detectors, more can be added to this work to further its usefulness to the scientific community. These improvements simplify to four points: First, we must further our understanding of collective effects. We chose to neglect this oscillation effect due to the current incomplete understanding of its impact in the literature. Although this remains a sound decision for this project as explained in 2, it provides us with only an incomplete picture. Second, the run time for Chimera supernovae simulations should be extended. MSW effects at the high resonance region on neutrino oscillations occur at a distance and time greater than that reached by the current Chimera simulations. In order to include MSW effects at the high resonance, we must extend the 2D and 3D simulations longer. Third, this work makes use of Chimera data on neutrinos that are "angle averaged" (i.e. neutrino luminosity is averaged over all angles for that particular simulation). To build a complete picture of neutrino luminosities during a supernova, this data should be collected along each line of sight. This would allow for an extremely detailed study of neutrino luminosities during a supernova at each line of sight. Lastly, the SNOwGLoBES software (Beck et al., 2013) makes use of an energy grid ranging from 0-100 MeV. To meet this requirement, we are forced to neglect the high energy neutrino luminosities generated by the Chimera code. It was pointed out in Chapter 2 that this was not a terrible approximation as there are simply very few neutrinos being detected at higher energies and so do not affect the overall number being detected. This should be tested by including all data generated by Chimera and compared to the results presented in this work.

Bibliography

(2012). *Fundamental Physics at the Intensity Frontier*. vii, 23

Abe, K. et al. (2011). Letter of Intent: The Hyper-Kamiokande Experiment — Detector Design and Physics Potential —. 11

Akiri, T. et al. (2011). The 2010 Interim Report of the Long-Baseline Neutrino Experiment Collaboration Physics Working Groups. 11

Beck, A., Beroz, F., Carr, R., Duan, H., Friedland, A., Kaiser, N., Kneller, J., Moss, A., Reitzner, D., Scholberg, K., Webber, D., and Wendell, R. (2013). *SNOwGLoBES: SuperNova Observatories with GLoBES: DRAFT*. v, vii, 1, 10, 14, 21, 51, 52

Becker-Szendy, R. et al. (1993). Imb-3: A large water cerenkov detector for nucleon decay and neutrino interactions. *Nucl. Instrum. Meth.*, A324:363–382. 11

Borne, J., Busto, J., Campagne, J.-E., Dracos, M., Cavata, C., Dolbeau, J., Duchesneau, D., Dumarchez, J., Gorodetzky, P., Katsanevas, S., Longhin, A., Marafini, M., Mezzetto, M., Mosca, L., Tonazzo, A., Patzak, T., Vassilopoulos, N., Volpe, C., Zghiche, A., and Zito, M. (2011). The memphys project. *Nuclear Instruments and Methods in Physics Research Section A: Accelerators, Spectrometers, Detectors and Associated Equipment*, 639(1):287 – 289. Proceedings of the Seventh International Workshop on Ring Imaging Cherenkov Detectors. 11

Boyd, R. N., Murphy, A. S. J., and Talaga, R. L. (2003). OMNIS, The Observatory for multiflavor neutrinos from supernovae. *Nucl. Phys.*, A718:222–225. [,201(2002)]. 12

Brandt, T. D., Burrows, A., Ott, C. D., and Livne, E. (2011). Results from core-collapse simulations with multi- dimensional, multi-angle neutrino transport. *The Astrophysical Journal*, 728(1):8. 8

Bruenn, S. W., Mezzacappa, A., Hix, W. R., Blondin, J. M., Marronetti, P., Messer, O. E. B., Dirk, C. J., and Yoshida, S. (2009). Mechanisms of core-collapse supernovae & simulation results from the chimera code. In Giobbi, G., Tornambe, A., Raimondo, G., Limongi, M., Antonelli, L. A., Menci, N., and Brocato, E., editors, *American Institute of Physics Conference Series*, volume 111 of *American Institute of Physics Conference Series*, pages 593–601. 9, 15

Bueno, A., Gil Botella, I., and Rubbia, A. (2003). Supernova neutrino detection in a liquid argon tpc. 12

Buras, R., Rampp, M., Janka, H.-T., and Kifonidis, K. (2003). Improved models of stellar core collapse and still no explosions: What is missing? *Physical Review Letters*, 90(24):241101. 9

Burrows, A. (1990). Neutrinos from supernova explosions. *Annual Review of Nuclear and Particle Science*, 40(1):181–212. 8

Cadonati, L., Calaprice, F. P., and Chen, M. C. (2002). Supernova neutrino detection in borexino. *Astropart. Phys.*, 16:361–372. 12

Chakraborty, S., Fischer, T., Mirizzi, A., Saviano, N., and Tomàs, R. (2011). No collective neutrino flavor conversions during the supernova accretion phase. *Phys. Rev. Lett.*, 107:151101. 21

Chiu, S. H., Huang, C.-C., and Lai, K.-C. (2013). Signatures of the neutrino mass hierarchy in supernova neutrinos. *PTEP*, 2015(6):063B01. 22, 24

Claeys, J. S. W., de Mink, S. E., Pols, O. R., Eldridge, J. J., and Baes, M. (2011). Binary progenitor models of type iib supernovae. *Astronomy and Astrophysics*, 528:A131. 3

Colella, P. and Woodward, P. R. (1984). The piecewise parabolic method (ppm) for gas-dynamical simulations. *Journal of Computational Physics*, 54:174–201. 9

Deserno, M. (2004). Linear and logarithmic interpolation. 18

Dighe, A. (2008). Physics potential of future supernova neutrino observations. *J. Phys. Conf. Ser.*, 136:022041. 22

Dighe, A. S. and Smirnov, A. Yu. (2000). Identifying the neutrino mass spectrum from the neutrino burst from a supernova. *Phys. Rev.*, D62:033007. 21, 22, 24, 25

Duan, H. and Kneller, J. P. (2009). Neutrino flavour transformation in supernovae. *Journal of Physics G: Nuclear and Particle Physics*, 36(11):113201. 8

Eguchi, K. et al. (2003). First results from kamland: Evidence for reactor anti-neutrino disappearance. *Phys. Rev. Lett.*, 90:021802. 12

Elias-Rosa, N., Dyk, S. D. V., Li, W., Miller, A. A., Silverman, J. M., Ganeshalingam, M., Boden, A. F., Kasliwal, M. M., Vink, J., Cuillandre, J.-C., Filippenko, A. V., Steele, T. N., Bloom, J. S., Griffith, C. V., Kleiser, I. K. W., and Foley, R. J. (2010). The massive progenitor of the type ii-linear supernova 2009kr. *The Astrophysical Journal Letters*, 714(2):L254. 3

Engel, J., McLaughlin, G. C., and Volpe, C. (2003). What can be learned with a lead based supernova neutrino detector? *Phys. Rev.*, D67:013005. 12

Fuller, G. M., Haxton, W. C., and McLaughlin, G. C. (1999). Prospects for detecting supernova neutrino flavor oscillations. *Phys. Rev.*, D59:085005. 12

Hargrove, C., Batkin, I., Sundaresan, M., and Dubeau, J. (1996). A lead astronomical neutrino detector: Land. *Astroparticle Physics*, 5(2):183 – 196. 12

Hillebrandt, W., Janka, H.-T., and Müller, E. (2006). How to blow up a star. *Scientific American*, 295 Number 4:43–49. vii, 4

Hirata, K. S., Inoue, K., Ishida, T., Kajita, T., Kihara, K., Nakahata, M., Nakamura, K., Ohara, S., Sato, N., Suzuki, Y., Totsuka, Y., Yaginuma, Y., Mori, M., Oyama, Y., Suzuki, A., Takahashi, K., Yamada, M., Koshiba, M., Nishijima, K., Suda, T., Tajima, T., Miyano, K., Miyata, H., Takei, H., Fukuda, Y., Kodera, E., Nagashima, Y., Takita, M., Kaneyuki, K., Tanimori, T., Beier, E. W., Feldscher, L. R., Frank, E. D., Frati, W., Kim, S. B., Mann, A. K., Newcomer, F. M., Van Berg, R., and Zhang, W. (1991). Real-time, directional measurement of ^{8}B solar neutrinos in the kamiokande ii detector. *Phys. Rev. D*, 44:2241–2260. 11

Huber, P., Lindner, M., and Winter, W. (2005). Simulation of long-baseline neutrino oscillation experiments with globes (general long baseline experiment simulator). *Comput. Phys. Commun.*, 167:195. 10, 14

Ikeda, M. et al. (2007). Search for Supernova Neutrino Bursts at Super-Kamiokande. *Astrophys. J.*, 669:519–524. 11

Janka, H.-T., Langanke, K., Marek, A., Martinez-Pinedo, G., and Mueller, B. (2007). Theory of core-collapse supernovae. *Phys. Rept.*, 442:38–74. vii, 7, 21

Kiewe, M., Gal-Yam, A., Arcavi, I., Leonard, D. C., Emilio Enriquez, J., Cenko, S. B., Fox, D. B., Moon, D.-S., Sand, D. J., Soderberg, A. M., and CCCP, T. (2012). Caltech core-collapse project (cccp) observations of type iin supernovae: Typical properties and implications for their progenitor stars. *Astrophysical Journal*, 744:10. 3

Kitaura, F. S., Janka, H.-T., and Hillebrandt, W. (2006). Explosions of o-ne-mg cores, the crab supernova, and subluminous type ii-p supernovae. *Astron. Astrophys.*, 450:345–350. 6

Kneller, J. (2015). personal communication. 22, 24

Lentz, E. J., Bruenn, S. W., Hix, W. R., Mezzacappa, A., Messer, O. E. B., Endeve, E., Blondin, J. M., Harris, J. A., Marronetti, P., and Yakunin, K. N. (2015).

Three-dimensional core-collapse supernova simulated using a 15 $m_\odot$ progenitor. *The Astrophysical Journal Letters*, 807:L31. v, vii, 1, 9, 14, 15, 16, 28, 51

Li, W., Leaman, J., Chornock, R., Filippenko, A. V., Poznanski, D., Ganeshalingam, M., Wang, X., Modjaz, M., Jha, S., Foley, R. J., and Smith, N. (2011). Nearby supernova rates from the lick observatory supernova search - ii. the observed luminosity functions and fractions of supernovae in a complete sample. *Monthly Notices of the RAS*, 412:1441–1472. 2

Limongi, M. and Chieffi, A. (2006). The nucleosynthesis of 26al and 60fe in solar metallicity stars extending in mass from 11 to 120 m: The hydrostatic and explosive contributions. *The Astrophysical Journal*, 647(1):483. 5

Lund, T. and Kneller, J. P. (2013). Combining collective, msw, and turbulence effects in supernova neutrino flavor evolution. *Phys. Rev.*, D88(2):023008. 22

Lund, T., Marek, A., Lunardini, C., Janka, H.-T., and Raffelt, G. (2010). Fast time variations of supernova neutrino fluxes and their detectability. *Phys. Rev. D*, 82:063007. 8

Marek, A., Dimmelmeier, H., Janka, H.-T., Müller, E., and Buras, R. (2006). Exploring the relativistic regime with newtonian hydrodynamics: an improved effective gravitational potential for supernova simulations. *Astronomy and Astrophysics*, 445:273–289. 9

MATLAB (2015). *version 8.5.0.197613 (R2015a)*. The Mathworks Inc., Natick, Massachusetts. 14, 17

Miller, A. A., Chornock, R., Perley, D. A., Ganeshalingam, M., Li, W., Butler, N. R., Bloom, J. S., Smith, N., Modjaz, M., Poznanski, D., Filippenko, A. V., Griffith, C. V., Shiode, J. H., and Silverman, J. M. (2009). The exceptionally luminous type ii-linear supernova 2008es. *The Astrophysical Journal*, 690(2):1303. 3

Mirizzi, A., Tamborra, I., Janka, H.-T., Saviano, N., Scholberg, K., Bollig, R., Hudepohl, L., and Chakraborty, S. (2015). Supernova neutrinos: Production, oscillations and detection. 21

Monzani, M. E. (2006). Supernova neutrino detection in borexino. *Nuovo Cim.*, C29:269–280. 12

Müller, E. and Steinmetz, M. (1995). Simulating self-gravitating hydrodynamic flows. *Computer Physics Communications*, 89:45–58. 9

O'Connor, E. P. (2012). *Topics in Core-Collapse Supernova Theory: The Formation of Black Holes and the Transport of Neutrinos*. PhD thesis, California Institute of Technology. 2, 8

Ott, C. D., Abdikamalov, E., O'Connor, E., Reisswig, C., Haas, R., Kalmus, P., Drasco, S., Burrows, A., and Schnetter, E. (2012). Correlated gravitational wave and neutrino signals from general-relativistic rapidly rotating iron core collapse. *Phys. Rev. D*, 86:024026. 8

Paxton, B., Bildsten, L., Dotter, A., Herwig, F., Lesaffre, P., and Timmes, F. (2011). Modules for experiments in stellar astrophysics (mesa). *The Astrophysical Journal Supplement Series*, 192(1):3. 5

Raffelt, G. G., Keil, M. T., Buras, R., Janka, H.-T., and Rampp, M. (2003). Supernova neutrinos: Flavor-dependent fluxes and spectra. In *Neutrino oscillations and their origin. Proceedings, 4th International Workshop, NOON2003, Kanazawa, Japan, February 10-14, 2003*, pages 380–387. 17

Scholberg, K. (2012). Supernova neutrino detection. *Annual Review of Nuclear and Particle Science*, 62:81–103. 11

Scholberg, K. (2012). Supernova neutrino detection. *Journal of Physics: Conference Series*, 375(4):042036. 13

Smartt, S. J., Eldridge, J. J., Crockett, R. M., and Maund, J. R. (2009). The death of massive stars - i. observational constraints on the progenitors of type ii-p supernovae. *Mon. Not. Roy. Astron. Soc.*, 395:1409. 2

Woosley, S. E., Eastman, R. G., Weaver, T. A., and Pinto, P. A. (1994). Sn 1993j: A type iib supernova. *Astrophysical Journal*, 429:300–318. 3

Woosley, S. E., Heger, A., and Weaver, T. A. (2002). The evolution and explosion of massive stars. *Rev. Mod. Phys.*, 74:1015–1071. 5

Zach, J. J., Murphy, A. S. J., Marriott, D., and Boyd, R. N. (2002). Optimization of the design of omnis, the observatory of multiflavor neutrinos from supernovae. *Nucl. Instrum. Meth.*, A484:194–210. 12

Vita

Tanner Devotie was born on June 27, 1989 in Knoxville, Tennessee to then Pamela Howard (now Devotie). He lived the first 24 years of his life in New Market, TN on a small family owned farm. It was during this time he attended Jefferson County High School in Dandridge, TN until 2007. Afterward, he attended Walters State Community College where he began his tutelage in physics under Dr. Samuel Morgan, a former NASA astrophysics department director. In 2010, Tanner Devotie graduated "cum laude" from W.S. with an A.S. in Physics. From there, Tanner attended the University of Tennessee to study physics further. In 2013, he graduated from U.T., earning a B.S. in Physics with a concentration in astrophysics. Finally, in the fall of 2013, he began his graduate career at the University of Tennessee to study astrophysics under the guidance of Dr. Otis (Bronson) Messer. He will earn his M.S. in Physics in December of 2015 with a concentration in astrophysics.